Acoustic impedance estimation from combined harmonic reconstruction and interval velocity

Luca Bianchin*, **Emanuele Forte***, **Michele Pipan***

**Dipartimento di Matematica e Geoscienze, Università di Trieste*

Via E. Weiss 1, Trieste, Italy

E-mail: luca.bianchin@phd.units.it; eforte@units.it; pipan@units.it

(February 10, 2019)

GEO-2018-0296

Running head: **AR AI estimation with velocity field**

ABSTRACT

Low-frequency components of reflection seismic data are of paramount importance for acoustic impedance inversion, but they typically suffer from a poor signal-to-noise ratio. The estimation of low frequencies of the acoustic impedance can benefit from the combination of a harmonic reconstruction method (based on autoregressive models) and a seismic-derived interval velocity field. We propose the construction of a convex cost-function that accounts for the velocity field, together with geologic a priori information on acoustic impedance and its uncertainty, during the autoregressive reconstruction of the low frequencies. The minimization of this function allows one to reconstruct sensible estimates of low-frequency components of the subsurface reflectivity, which lead to an estimation of acoustic impedance model via a recursive formulation. In particular, the method is suited for an initial and computationally inexpensive assessment of the absolute value of acoustic impedance even

when no well log data are available. We first tested the method on layered synthetic models, then we analyzed its applicability and limitations on a real marine seismic dataset that included tomographic velocity information. Despite a strong trace-to-trace variability in the results, which could partially be mitigated by multi-trace inversion, the method demonstrates its capability to highlight lateral variations of acoustic impedance that cannot be detected when the low frequencies only come from well log information.

INTRODUCTION

This paper describes a 1-D post-stack methodology that aims at inferring the acoustic impedance (AI) of the subsurface from amplitudes of seismic records and ancillary information that may be available in the aftermath of a seismic survey. The trace-by-trace approach discussed here is a simplification of the general problem of seismic waveform inversion. Our approach implies a computationally inexpensive algorithm that can be useful for an initial assessment of the subsurface acoustic properties. The subsurface AI model is reconstructed by assuming an acoustic isotropic propagation medium. Low frequencies of this model are ill-conditioned components of the solution because of the poor S/N that active-source seismic data exhibit at low frequencies. Typically, when dealing with seismic data for oil and gas exploration, frequencies below 5-10 Hz are strongly affected by acquisition and environmental noise (e.g. Lesage et al. (2015)). Broadband seismic data acquired in recent years, show a good S/N starting from frequencies as low as 2.5 Hz (Soubaras and Lafet, 2011). Regardless, our method remains useful for conventional, as well as for higher resolution seismic data.

Veeken and Da Silva (2004) provide an overview of several inversion methods for the recovery of noisy low frequencies. We propose a modification of the autoregressive (AR) method (Walker and Ulrych, 1983) in which we constrain the AR inversion using a seismic-based velocity field. We call this approach combined AR-velocity (CARV) method. The AR reconstruction of reflectivity allows one to recursively compute a full bandwidth AI estimate (Russell, 1988). The AR low frequency reconstruction method was originally proposed together with the minimum L1-norm solution (Oldenburg et al., 1983) in the 1980's. The latter solution found larger success with the advent of fast algorithms (i.e. Iterative Reweighted Least Squares) in the field of linear programming. Minimum L1 or L1/L2 norm

solutions do not require a spectral estimation with its associate sources of error. Rather, these solutions make a different a priori assumption: that of a sparse time domain representation of reflectivity (Walden and Hosken, 1985). In this respect, they produce different AI models than the ones identified by the AR reconstruction. More recently, Gholami and Sacchi (2013) achieved a sparse solution by minimizing the total variation of AI rather than performing the reconstruction in reflectivity domain. Many other methods for bandwidth extension have been proposed to date but we limit our analysis to the harmonic extrapolation methods for a physically valid quantitative reconstruction of the acoustic properties. A careful analysis on the validity of the AR and sparse spike reconstruction, compared to other methods is detailed by Liang et al. (2017).

The AR method for impedance inversion is a model-based method. This method predicts the low frequency components of each seismic trace by fitting an AR model to the frequency components that show an adequate S/N. The AR model assumes the signal to be composed of a limited number of events in time domain. A limited number of events in time domain corresponds to a limited number of complex sinusoids in the Fourier domain and in turn to a blocky AI. By assuming that the trace is made up of a limited number of reflections, ill-conditioned low frequency components of reflectivity are univocally reconstructed to be consistent to the components measured in the band-pass region. The reconstruction is based on the extension of few sinusoids estimated from the data, hence the term harmonic. The reconstruction makes use of the conjugate symmetry of real signals in the Fourier domain. The reconstruction is deterministic because the inverted output consists of only a single model among many that fit the data. The deterministic nature of the estimate proposed does not prevent the undertaking of a sensitivity analysis on the parametrization adopted. The most relevant parameters to consider are the relevance of the interval velocity field in

the estimate, the number of reflection events to be modeled, and the frequency band in which the AR model is estimated.

THEORY

In order to obtain a sensible absolute AI inversion the input seismic trace must be properly processed to include only primary energy. Effects of source and receiver signatures must be accounted for and removed during processing. Accurate imaging is required to place seismic events at their true subsurface locations before inversion. The inversion algorithm proposed here does not account for non-zero incidence angles; therefore the input post-stack data should ideally be a near-angle partial stack. The choice of angles has to be a trade-off between data quality, which is related to stacking fold, and the offset required to achieve such fold. Alternatively, the AVO intercept section could be used as input for the reconstruction. This approach implies that the AVO behavior of the data is properly modeled, which could be problematic when strong anisotropic or higher order effects are present in the records. Relative amplitudes of the events must be preserved throughout processing. Since often the relative amplitude is preserved but the processing is not actually "true amplitude", we invoked a global scalar for the whole seismic section. In absence of accurate well log ties, the scalar can be approximately determined from the a priori knowledge of AI at two different depths and applied to the data before inversion.

The convolutional model (Robinson, 1954), is at the root of the impedance inversion method proposed in this paper. This model assumes that the processed seismic trace $d(t)$ can be expressed as:

$$d(t) = w(t) * r(t) + n(t), \tag{1}$$

where $w(t)$ is a time-invariant seismic wavelet, $r(t)$ is the reflectivity series providing information on the subsurface features of interest and $n(t)$ is the additive noise, which includes all the features of the data that cannot be ascribed to the previous two terms.

Dispersion and attenuation are not taken into account by the convolutional model as well as by the proposed algorithm. In order to uniquely single out the interfaces between layers of contrasting AI, we make three assumptions: weak dispersion, sparsity of reflectivity (Oldenburg et al. (1983) and Hargreaves et al. (2013)), and high frequency (i.e. Bleinstein et al. (2000) pp. 5-6). The high frequency approximation assumes that the rock property variations have much longer wavelength than the longest wavelength of the seismic source. In the presence of thin layers, the AR method is expected to fail, and the absolute value of the predicted AI to be biased below the layers whose thickness is similar to that of the seismic wavelength (see Figure 1 at about traces 2-10 for reference). This behavior is well known (Ulrych and Walker, 1984), and additional information (interval velocity field and a priori geologic constraints) is required to increase the accuracy of the inversion in the real case scenarios that may not meet the three assumptions. Figure 1 exemplifies the effects of the bias that may be introduced when thin layers are inverted for the AI with an unconstrained AR approach.

Figure 1 about here.

The seismic traces that meet the assumptions described above, having been band-pass filtered to reject the noisier spectral components (including the low frequencies), can be

modeled as:

$$d'(t) = sr'(t) + n'(t), \tag{2}$$

where $d'(t)$ is the bandlimited seismogram, s is a scalar, $r'(t)$ is a bandlimited version of reflectivity and $n'(t)$ represents the bandlimited component of noise. After such processing, the seismic traces represent a scaled and noisy bandlimited reflectivity series. Data must be processed to zero phase in order to place the interfaces between adjacent layers at their correct temporal position. Approximate results can also be obtained without properly removing the wavelet effects. However the results depart from the theoretic reconstruction in such a way that the resulting very low frequencies are completely unreliable if no accurate constraints at depth are imposed in the inversion (see appendix A). A time variant AR process (Rao, 1970) may model the complex-value non stationary series in this case. Tary et al. (2014) provide a detailed description on the topic of fitting time variant AR models on seismic time series, but such models have not been considered in this paper. Provided that equation 2 is valid and as long as the scalar s is properly estimated and noise taken into account, the input data for the inversion may be $d'(t)$ or $r'(t)$. The reconstruction performed in the zero-offset data domain is a scaled version of the reconstruction performed in the reflectivity domain. In what follows, the data in the band-pass window will be modeled by equation 2, which provides a means to estimate $r'(t)$ from the data. The reflectivity thus obtained becomes the input to the inversion process. We follow the weak contrast approximation introduced by Peterson et al. (1955) to relate the AI to the interface property of reflectivity (r_i) for a continuous earth model and normal incidence:

$$AI(t) = AI(t_0)e^{2\sum_{i=1}^{t} r_i}. \tag{3}$$

If the reference impedance is known or estimated at a certain depth $AI(t_{ref})$ rather than near the surface ($AI(t_0)$), the AI reconstruction above the reference level is obtained by

rewriting equation 3 as:

$$AI(t) = \frac{AI(t_{ref})}{e^{2\sum_{i=t_0}^{t} r_i}}. \tag{4}$$

In case the absolute value of reflectivity is smaller than 0.4, the difference between the results of equation 3 and the formulation of impedance for a discrete layered earth,

$$AI(t) = AI(t_0) \sum_{i=t_0}^{t} \frac{1+r_i}{1-r_i}, \tag{5}$$

is negligible for a single interface (Bertheussen and Ursin, 1993) but the difference accumulates for increasing depths proportionally to the sum of the cubic power of the amplitudes of each event. All the frequency components of the reflectivity must be available to invert for the absolute value of AI by using equation 3 or 4. In particular, the low frequency components of reflectivity play the most relevant role in describing the features of AI because of the low frequency boosting due to the summation operator in equation 3 or 4.

METHOD

The proposed method estimates the absolute AI by considering the spectrum of each post-stack seismic trace as a gapped complex signal. The gap refers to the low frequency part of the recorded data that is bounded by the negative and positive signal spectral components. The idea of filling the gap was initially proposed by Fahlman and Ulrych (1982) in the context of power spectral estimation and developed by Walker and Ulrych (1983) for the case of seismic inversion. The novelty of the proposed approach consists of including, during the gap filling process, information from interval velocity together with geologic knowledge on impedance and its uncertainty. The inclusion of ancillary information is performed by modifying the original formulation proposed by Walker and Ulrych (1983).

Harmonic representation of times series

The harmonic AR modeling is fully detailed in Walker and Ulrych (1983) and we will only outline here the salient points that may be useful for the new aspects of the proposed CARV inversion. A limited number (M) of events in a recorded time series is represented in the Fourier domain (R_f) by a sum of a limited number of complex sinusoids in a noise-free case

$$R_f = \sum_{k=1}^{M} r_k e^{-i2\pi f \tau_k}. \tag{6}$$

In equation 6 τ_k represents the travel-time of the events r_k. A limited number of sinusoids is fully described by a linear combination of M Fourier components

$$R_f = \sum_{k=1}^{M} R_{f-k} e^{-i2\pi k \tau_k}. \tag{7}$$

Equation 7 can be interpreted as perfectly predictable AR process of coefficients g_k and innovation equal to 0:

$$R_f = \sum_{k=1}^{M} g_k R_{f-k}. \tag{8}$$

Innovation, in the context of AR modeling, describes the unpredictable part of the process as the difference between the recorded value and the value predicted by the harmonic model (Kay and Marple, 1981).

ARMA models for noisy data

In the presence of noise (N_f) that is uncorrelated to signal (R_f) in the recorded data (X_f), an autoregressive moving average (ARMA) process with the same coefficients for the AR and the moving average process is the correct representation of the signal (Ulrych and Clayton, 1976):

$$R_f = X_f - N_f = \sum_{k=1}^{M} g_k X_{f-k} - \sum_{k=1}^{M} g_k N_{f-k}. \tag{9}$$

The spectral estimator of Pisarenko (1972) can be used to fit an ARMA model to the data. However, this method is very sensitive to the model order (Kay and Marple, 1981), which must be chosen to be equal to the number of the reflections plus one: this piece of information is not available a priori in real case scenarios. A modification of the Pisarenko method that makes use of projection filters (Soubaras, 1994) has been proposed by Sacchi and Kuehl (2005). This approach provides an estimate of all the R_f in equation 9 as

$$\mathbf{R} = (\mathbf{Id} - (\mathbf{G}^H\mathbf{G} + \psi\mathbf{Id})^{-1}\mathbf{G}^H\mathbf{G})\mathbf{X}, \tag{10}$$

where $\mathbf{G}$ is the convolution matrix of the coefficients of the Prediction Error Operator ($\mathbf{g}^H\mathbf{g}$) and ψ is a regularization parameter to account for the magnitude of the noise variance when its distribution is assumed to be Gaussian (Chen and Sacchi, 2014). The vector $\mathbf{R}$ estimated from equation 10 is in theory the noise-free spectral representation of a limited number of events in the time representation of the seismic trace (Sacchi and Ulrych, 2005). The noise-free estimate can be used as input for the AR reconstruction of low frequencies.

AR low frequency reconstruction

AR models of order much longer than the number of complex sinusoids in the data mimic the ARMA behavior and can be adopted to reduce the sensitivity of the results to the model order in the presence of noise (Walker and Ulrych, 1983). Figure 2 (which is described more fully in the RESULTS section) compares the AR reconstruction to the ARMA reconstruction of the full bandwidth of a synthetic sparse time series. In order to fill the low frequency gap with an AR model, Walker and Ulrych (1983) minimize the AR forward and backward prediction error in the following cost function

$$\min_{R_{Lf}} ||\sum_{k=0}^{M} g_k R_{f-k}||_2^2 + ||\sum_{k=0}^{M} g_k^H R_{f+k}||_2^2 = \min_{R} ||\mathbf{CR} - \mathbf{b}||_2^2. \tag{11}$$

The vector **R** contains the low frequency components of the reflectivity spectrum, the matrix **C** contains the convolution of the AR coefficients, and the vector **b** describes the known terms resulting from the multiplication of the AR coefficients and the known Fourier components of the spectrum at higher frequencies. An explicit solution is found by imposing the first derivative of equation 11 with respect to **R** equal to 0:

$$\begin{pmatrix} 2|\sum_{k=-M}^{M} g_k g_k^H R_{f+k}| \\ \dots \\ 2|\sum_{k=-M}^{M} g_k g_k^H R_{-f+k}| \end{pmatrix} = \begin{pmatrix} 0 \\ \dots \\ 0. \end{pmatrix} \tag{12}$$

The minimization of equation 11 is a two-stage process: the AR filter coefficients (g_k) are initially estimated from a spectral window where the wavelet effects are properly removed and, after the gap of low frequencies is filled, a new AR model is fitted to the original spectral window plus the low frequency band to return an updated version of the low frequency reconstruction. This procedure reduces the prediction error (Fahlman and Ulrych, 1982). The computation of the autocorrelation function on a longer complex-value series is one of the factors to account for the reduction in the prediction error when the second AR model is fitted to the gap-filled spectrum. This approach helps to stabilize the estimation of the later lags of the autocorrelation that are particularly relevant for the estimation of the AR coefficients when the order of the AR model is close to the length of the spectral passband. Different spectral estimators lead to different reconstructions of the AR coefficients. This behavior is particularly relevant in presence of a large number of reflectors and interference features. In this paper the Yule-Walker (Kay and Marple, 1981) method has been applied, providing more stable results when applied to both complex synthetic scenarios and real data.

The spectral components that show a poor S/N are not suitable for quantitative inversion in the framework of AR models (Kay and Marple, 1981). Following the work of Walker

and Ulrych (1983) we define a frequency band where S/N is adequate for inversion. The average amplitude spectrum of the input seismic section can be used to estimate reasonable cut-off frequencies. The choice is a trade-off between neglecting part of the information present in the data and estimating the model on a flat part of the spectrum, where the signal prevails over the noise. The choice of low- and high-cut frequency (passband length) also influences the order of the AR model that best describes the data. Walker and Ulrych (1983) recommend an AR model order which is 0.7 times the passband length (in units of sampled frequencies) on the real data tested. Our tests confirm this empiric rule. Such recommendation implies that as the passband length shortens, the AR model also shortens, and therefore fewer features of impedance variation can be accurately obtained by the model (Hendrick and Hearn, 1993). To overcome the incorrect predictions due to the AR reconstruction only, we introduce in the CARV algorithm the information coming from the interval velocity field.

Interval velocity field

We do not discuss here all the various methods to obtain an accurate seismic-based interval velocity field, and we only consider the velocity field as an input for our algorithm. In order to tie the reconstruction of AI to the velocity field, a rock physics expression for the density term has to be assumed. Gardner et al. (1974) or other empirical relationships can be adopted. With the first choice, and following the notation of Oldenburg et al. (1983)

$$\rho(t) = C v_p(t)^{\alpha} \tag{13}$$

where $\rho(t)$ is the bulk density, $v_p(t)$ the p-wave velocity, C and α are two scalars. The AI can consequently be estimated by the following expression:

$$AI(t) = Cv_p(t)^{1+\alpha}. \tag{14}$$

The coefficient α is typically much smaller than 1 leading to a quasi-linear propagation of the error from the interval velocity field to the AI obtained from equation 14.

Many prospects of interest for oil and gas exploration show anomalous deviations from Gardner's trend. Löseth et al. (2011) describe this issue with particular emphasis on the amount of organic content in source rocks. In our method the velocity field information is not incorporated as a series of constraints (Oldenburg et al., 1984), but rather as a weight in the inverse problem. The use of the weight provides flexibility to the solution and the possibility to emphasize anomalies on Gardner's trend due to the seismic reflection information. The interval velocities we consider contain very-low-frequency information. Most of the velocity fields derived from conventional seismic tomography show significant spectral content until 2 Hz (ten Kroode et al., 2013), but factors related to target depth, offset length and velocity variations may imply a higher resolution. We chose to sample the velocity field at the sampling rate corresponding to the low frequency cut-off chosen for the seismic passband. This choice is generally safe with respect to the spectral content of the velocity field and, providing there is no aliased energy, larger sampling intervals can be chosen to improve the algorithm performance. Each of the re-sampled values of the velocity field is transformed into AI by using equation 14. Ulrych and Walker (1984) provide a relationship to tie the low frequency components of the reflectivity (${R_L}^f$) to the values of impedance at depth in the form of

$$\begin{aligned} \log \tfrac{AI(t)}{AI(0)} - 2\int_{t_0}^{t_k} r^H(u)du = 2\int_{t_0}^{t_k} r^L(u)du = 2\int_{t_0}^{t_k} \textstyle\sum_{f=-Fmin}^{Fmax} R_L^f e^{-i2\pi fu}du = \\ = \textstyle\sum_{f=-Fmin}^{Fmax} R_L^f 2\int_{t_0}^{t_k} e^{-i2\pi fu}du. \end{aligned} \tag{15}$$

In equation 15 ($r^H(u)$) is a known term that describes the time-domain reflectivity components within the passband. t_k is the time corresponding to the k-th velocity-derived recommendation for the AI. The continuous approximation of the reflectivity integral for a discrete time series allows the analytical solution of equation 15 as

$$\log \frac{AI(t)}{AI(0)} - 2\int_{t_0}^{t_k} r^H(u)du = \sum_{f=-Fmin}^{Fmax} R_L^f (2\frac{e^{i2\pi f t_k}}{i2\pi f} - 2\frac{e^{i2\pi f t_0}}{i2\pi f}). \tag{16}$$

The unknowns for both equation 15 and 16 are R_f^L. All the equations described in the system 16 are linear with respect to the unknowns R_f^L and can be rewritten in matrix notation as

$$\boldsymbol{\gamma} = \mathbf{LR}. \tag{17}$$

In equation 17, $\boldsymbol{\gamma}$ describes the known terms, $\mathbf{L}$ represents the Inverse Fourier transform combined with the integration operator, and $\mathbf{R}$ is the vector of low-frequency reflectivity. The smaller the Euclidean norm of the residual $||\mathbf{LR} - \boldsymbol{\gamma}||_2^2$, the closer the estimated reflectivity is to the information provided by the velocity field.

A priori geologic constraints

Seismic data acquisition normally follows a preliminary geologic assessment of the region of interest. For this reason, constraints on AI at different depths are generally available on a geologic basis. The accuracy of such constraints depends on the degree of knowledge of the surveyed area. Equation 15 describes a way to introduce equality constraints ("hard constraints") on impedance into the AR solution. To account not only for the value of impedance at depth but also for its uncertainty, "soft constraints" are proposed for application to each trace of a 2D section or a 3D seismic volume. By soft constraints we refer to constraints that provide an upper an a lower bound to the AI inversion at selected

depths. When the unconstrained AR reconstruction produces an AI inversion that does not fit within the impedance constraint limits, the AR method is modified such as the vector $\mathbf{R}$ from equation 11 is no longer the one that minimizes the AR prediction error, but it is the one that minimizes the AR prediction error among those that fit the impedance constraint limits. In a probabilistic framework, the approach taken here imposes a uniform a priori probability distribution for the AI at selected depths within two bounds. This condition was not extensively explained in the original Ulrych and Walker (1984) publication. The uncertainty can both be in time and in the value of the AI. Small errors in defining the time of the constraints (of the order of tenths of temporal samples) can be tackled by evaluating the cost function proposed in equation 20 for the different combinations of the travel-times admitted by the timing uncertainty. The timings of the constraints that produce the minimum value of the cost function are then adopted. The use of large time uncertainties makes the constraints ineffective. On the other hand, to account for the uncertainty on the values of impedance constraints, equation 16 can be modified as it follows:

$$\begin{array}{l} \log\frac{AI(t)-\Delta AI(t)}{AI(0)} - 2\int_0^t r^H(u)du \leq \sum_{f=-Fmin}^{Fmax} R_L^f(2\frac{e^{i2\pi f t_k}}{i2\pi f} - 2\frac{e^{i2\pi f t_0}}{i2\pi f}) \\ \sum_{f=-Fmin}^{Fmax} R_L^f(2\frac{e^{i2\pi f t_k}}{i2\pi f} - 2\frac{e^{i2\pi f t_0}}{i2\pi f}) \leq \log\frac{AI(t)+\Delta AI(t)}{AI(0)} - 2\int_0^t r^H(u)du \end{array} . \quad (18)$$

$\Delta AI(t)$ represents the uncertainty on the AI. In a more compact form, equation 18 can be written as:

$$\begin{cases} \mathbf{HR} \leq \boldsymbol{\beta} + \boldsymbol{\Delta\beta} \\ -\mathbf{HR} \leq -\boldsymbol{\beta} + \boldsymbol{\Delta\beta} \end{cases} . \quad (19)$$

Equation 19, introduced by the background geologic knowledge, is a condition that can be included in a constrained optimization problem.

Inversion formulation

The CARV inversion proposed in its general form can be described by the minimization of the convex cost function:

$$J = ||\mathbf{CR} - \mathbf{b}||_2^2 + \lambda||\mathbf{LR} - \boldsymbol{\gamma}||_2^2 \qquad s.t. \quad \begin{cases} \mathbf{HR} \leq \boldsymbol{\beta} + \boldsymbol{\Delta\beta} \\ -\mathbf{HR} \leq -\boldsymbol{\beta} + \boldsymbol{\Delta\beta} \end{cases} \tag{20}$$

with respect to the vector $\mathbf{R}$ of low frequency components of reflectivity. The condition $\min_{\mathbf{R}} ||\mathbf{CR} - \mathbf{b}||_2^2$ comes from equation 11 and aims at minimizing the AR forward and backward prediction errors. The cost function includes the regularization term ($||\mathbf{LR} - \boldsymbol{\gamma}||_2^2$) to make the resulting low frequencies adhere to the AI estimated from the interval velocity field. The degree of adherence is controlled by the parameter $\lambda \geq 0$.

Sensible values for λ may come from the ratio between the maximum eigenvalues of the matrix $\mathbf{C}^H\mathbf{C} = \mathbf{G}$ (in Walker and Ulrych (1983) original notation) and $\mathbf{L}^H\mathbf{L}$, but the final choice depends on the relative confidence on the velocity field with respect to the confidence on the seismic amplitudes. The velocity field is the regularization term and the soft constraints on impedance can be implemented by a constrained least squares algorithm (i.e. via a subspace trust-region method). Minimizing equation 20 is equivalent to a multi-objective optimization problem:

$$\min_{\mathbf{R}} \nabla J = \mathbf{GR} - \mathbf{B} + \lambda(\mathbf{L}^H\mathbf{LR} - \mathbf{L}^H\boldsymbol{\gamma}) \qquad s.t. \quad \begin{cases} \mathbf{HR} \leq \boldsymbol{\beta} + \boldsymbol{\Delta\beta} \\ -\mathbf{HR} \leq -\boldsymbol{\beta} + \boldsymbol{\Delta\beta} \end{cases} \tag{21}$$

where $\mathbf{B} = \mathbf{C}^H\mathbf{b}$. The regularization term pertaining to the velocity field ($\mathbf{L}^H\mathbf{L}$) concentrates its information at the very low frequencies (around its main diagonal). This fact underlines the relevance of the velocity field term to weight the solution trend, while the AR term influence is stronger at higher frequencies within the low frequency gap. There is no mathematical guarantee that the matrix to be inverted $\mathbf{G} + \lambda\mathbf{L}^H\mathbf{L}$ is well conditioned,

although no issue has been found during testing on synthetic and real data. This experimental statement can be explained by the decaying nature of the autocorrelation function of seismograms that leads to the Toeplitz matrix $\mathbf{G}$ with largest values around its main diagonal. In case of instability during the inversion, additive white noise can be possibly introduced into equation 21 by summing a weighted identity matrix. We obtained stable low-frequency reconstructions for all the results presented in this paper without such regularization.

Inversion with lateral continuity

An unwanted feature in the inversion of real data is the trace-to-trace variability of the results. Many seismic amplitudes may be related to causes other than rock property-based reflectivity changes like interference, noise, residual wavelet effects and other inaccuracies in the processing flow. The integral operator that transforms reflectivities into AI magnifies the issue at the low-frequency end, leading to vertical stripes which are obviously not related to the actual properties of the subsurface materials. Ideally, we expect to find solutions that show some level of reasonable trace-to-trace stratigraphic continuity. This expectation is especially true for low-frequency components of AI, which should directly be related to smooth spatial changes in geology. To reduce the instability in the inverted AI, the data may be smoothed before inversion with a targeted processing that removes the incoherent noise. Alternatively, the cost function may be modified to promote the continuity of the solution, or a spatial low-pass filter can be applied after inversion. We focus here on modifying the cost function, with an additional penalty term related to the trace-to-trace variability of the reflectivity reconstruction. This penalty term only influences the low-frequency part of the spectrum that we aim at reconstructing. Provided that the impedance of the first layer is

constant for all the traces in the section, we obtain a laterally continuous AI by solving for the lateral variation of the low frequency components of the reflectivity ($\mathbf{\Delta R}$) rather than for $\mathbf{R}$ in equation 20. The cost function of equation 20 can be rewritten with an additive term $\mu\mathbf{Id\Delta R}$ (where $\mathbf{Id}$ represents the identity matrix):

$$J = ||\mathbf{C\Delta R} + \mathbf{CR_0} - \mathbf{b}||_2^2 + \lambda||\mathbf{L\Delta R} + \mathbf{LR_0} - \boldsymbol{\gamma}||_2^2 + \mu||\mathbf{Id\Delta R}||_2^2 \quad s.t. \begin{cases} \mathbf{HR} \leq \boldsymbol{\beta} + \mathbf{\Delta}\boldsymbol{\beta} \\ -\mathbf{HR} \leq -\boldsymbol{\beta} + \mathbf{\Delta}\boldsymbol{\beta} \end{cases}. \tag{22}$$

We call $\mathbf{R_0}$ the known term pertaining to the low frequency reconstruction at the previous adjacent-trace location. The additive term $\mu\mathbf{Id\Delta R}$ controls the amount of trace-to-trace variability ($\mu \geq 0$). Once $\mathbf{R_0}$ is arbitrarily chosen at both ends of the line, the low frequency components of reflectivity $\mathbf{R}$ can be iteratively obtained as $\mathbf{R} = \mathbf{R_0} + \Delta\mathbf{R}$ at each trace location. We perform the summation from one end of a seismic line to the other and in the opposite direction and we adopt the average of the two results as our smoothed AI estimate. In case a seismic cube is available, the summation operation could be performed in inline and cross-line direction separately, and then the results could be merged. Alternatively, slightly different penalty terms that weight the $\mathbf{\Delta R}$ term over many traces may be considered in equation 22 to produce a smooth inversion in one step only.

Reflectivity extension to high frequency

The high frequency components of the data are as unreliable as the very low frequencies, but note that the high frequency content of reflectivity tends to be suppressed when recursively summed into AI (see equation 3 or 4). Walker and Ulrych (1983) proposed to minimize an entropy norm (Ooe and Ulrych, 1979) after the low frequency completion to reconstruct the full bandwidth of reflectivity from its low-mid frequency content. We adopt, instead, a logarithmic entropy function with frequency domain constraints (Sacchi et al., 1994). Both

norms aim at obtaining a sparse solution compatible with the input time series. This approach agrees with the initial assumption that the algorithm recovers the full bandwidth of reflectivity given a limited number of events in the recorded traces. Minimizing an entropy norm as a final step of a constrained harmonic reconstruction process might lead to instabilities. Factors that may contribute to instability are the presence of noise and the presence of conflicting information between the velocity field and the geologic constraints. A further element that may contribute to instability is the parametrization of the minimum entropy deconvolution algorithm. The tolerance on the entropy norm increment at each algorithm iteration plays the most important role in determining the energy of the reconstructed high frequencies. A threshold ratio equal to one between the energy of the high-frequency components and the energy of the low-mid frequencies is adopted here to terminate the iterative high frequency reconstruction process. Our threshold choice has the purpose of limiting the high-frequency reconstruction impact on the inversion result. This approach is taken because we do not trust the quantitative outcome of the deconvolution process and we use the outcome of the deconvolution only as a mean to enhance the sharpness of the stronger reflectors for the purpose of obtaining a blocky AI inverted model. The application of this reconstruction step does not influence the validity of the low- and mid-frequency estimates of the AI.

RESULTS

In this section we illustrate the novel aspects and the performance of the proposed inversion method, with emphasis on describing general results rather than a data- or site-dependent behavior. For the sake of clarity, we summarize the various approaches to AI inversion that we will discuss on synthetic examples and real data in Table 1. All the AI inversion results

are expressed in rayl, corresponding to $kg/m^2/s$.

Table 1 about here.

Synthetic examples

We generated 1-D time series that simulate seismic traces to assess the effectiveness of the four reconstruction methods described in Table 1. The fifth method, the model-based approach, is introduced in the inversion of a real seismic dataset for comparison with the harmonic reconstruction methods. We assumed two input models, both characterized by a blocky impedance corresponding to a sparse time-domain reflectivity. Model 1 contains 10 vertically stacked AI blocks, while Model 2 contains 100 AI blocks. Both models are discretized into 1,000 temporal samples. The input synthetic data in Figure 2 is a bandlimited (8-70 Hz) version of the model reflectivity function with additional white noise (S/N=34 dB in terms of maximum amplitude). Figure 2 highlights the sensitivity of the unconstrained AR and ARMA reconstructions to the model order choice on the Model 1 synthetic example. No constraint at depth or velocity field regularization is required for obtaining reliable results on such a sparse and controlled synthetic example when the appropriate model order is chosen. The ARMA process that correctly models the data is of order 10, while we assume that the best AR approximation is obtained for a model order of 105 (in line with the recommendation of selecting the model order 0.7 times the passband length in units of sampled frequencies). Given a Nyquist frequency of 125 Hz, and a 12 to 50 Hz signal bandwidth choice, the number of sampled frequencies available for fitting the AR model is 152. When the ARMA model order is smaller than the actual number of events in the data (Figure 2B, model order 7), the reconstruction becomes unreliable

because the low-frequencies are incorrectly modeled. The instability of the ARMA model appears hard to overcome because one needs to know exactly the number of reflectors that are contained in the model before inverting the seismic section. Figures 2B and 2C show that the sensitivity of the impedance profile results is much lower for the AR than for the ARMA approach, despite the range of relative normalized order values being comparable between the two types of reconstruction. The comparison in Panel 2D between the two more accurate AR and ARMA solutions shows the good approximation, in presence of noise, of a long AR model to the appropriate ARMA model.

Figure 2 about here.

Synthetic Model 1 and Model 2 are compared in Figures 3, 4, and 5 to show the effectiveness of the CARV reconstruction with respect to the classical AR approach on a controlled input. In these Figures, panels A and B show the input synthetic data (7-80 Hz zero-phase Butterworth filter) on the Model 1 and Model 2 reflectivity with additional white noise (S/N=34 dB in terms of maximum amplitudes). Panels C and D are obtained after the low-frequency reconstruction and the subsequent AI inversion on the input trace of panels A and B, modified by the absence of additional white noise. Panels E and F are obtained from the reconstruction of the traces of panels A and B, respectively. We present in panels G and H the reconstruction results that can be obtained when the input trace is the convolution between the model reflectivity and a 30 Hz Ricker wavelet that bandlimits the data (no additive noise). Figure 3 shows the quality of the reconstruction that can be achieved with the unconstrained AR models, in comparison to the bias introduced by the weak con-

trast approximation. The weak-contrast approximation is not a relevant limitation for both Model 1 and Model 2 reconstructions: all panels of Figure 3 evidence the reduced bias of the unconstrained AR solution that can be imputed to this approximation. A bias in the reconstruction of the DC component of the AI is also clearly visible in Figures 3C to 3H. In fact, frequencies close to the DC component are generally the hardest to be successfully reconstructed by the AR model, as it has been reported since the work of Oldenburg et al. (1983). This behavior can be clearly seen as the AI drift, in particular for the more complex Model 2 (Figures 3D, 3F, and 3H). We propose the two reconstructions of panels 3G and 3H to highlight the effects of not correcting for the wavelet shape before performing the reconstruction. The wavelet effects on the reconstruction are visible both in terms of high frequency undesired features and low frequency drift in Figures 3G and 3H.

Figure 4 shows the effects of the soft constraints on impedance at selected times (blue brackets) that aim at limiting the bias introduced by incorrect AR predictions. As reported in Table 2, the RMS error between the input Models (red curves) and the constrained AR reconstructions (black curves), is smaller or equal to the RMS error between the input Models and the unconstrained AR reconstructions (gray curves). The reconstructions in Panels 3H and 4H represent no exception, but the absence of constraints in the shallow layers has the side effect of producing a less accurate reconstruction in the shallow part of the constrained solution (Figure 4H) then in the shallow part of the unconstrained solution (Figure 3H). An explanation for this behavior can be sought in the artifacts that are introduced when the wavelet shape is not removed before the low-frequency reconstruction. On the contrary, the drift from the input model is strongly reduced in Panels 4D and 4F with respect to Panels 3D and 3F. Figures 2 to 4 do not make use of the velocity field information. The effects and artifacts of incorporating an interval velocity field which does not have the AI blocky

structure are shown in Figure 5. The AI curve that plays the role of the velocity-derived AI field in Figures 5C, 5E and 5G is obtained by fitting, in a least squares sense, a polynomial of order 5 to the Model 1. The best fit polynomial of order 8 is used in Figures 5D, 5F, and 5H to derive the green AI curve for Model 2. The trade-off parameter λ that governs the amount of velocity-field derived AI in the inversion, has been chosen as 0.5 times the ratio between the maximum eigenvalues of matrix $\mathbf{G}$ and $\mathbf{L}^H\mathbf{L}$ for all the panels of Figure 5. In addition to the information coming from the velocity field, the constraints on impedance indicated by the blue brackets in Figure 5 have been enforced. The CARV reconstruction of Model 2 still shows a relevant mis-tie with respect to the reference AI model in the shallowest part (panels 5D, 5F, 5H). Weighting in the solution the low frequency AI model that mimics an AI model derived from a velocity field reduces the reconstruction error with respect to the results of panels 4D, 4F and 4H. Note that the CARV reconstruction of panel 5C appears less blocky than the reconstruction 4C that does not account for the velocity field: this is an unrealistic case in which the extreme sparseness of the layer interfaces and the absence of noise lead to a CARV inversion that is less blocky than the classical AR inversion.

Figure 3 about here.

Figure 4 about here.

Figure 5 about here.

Table 2 about here.

Figure 6 shows the amplitude spectrum of the reconstructed reflectivity whose derived AI is shown in Figure 5F, in comparison to the amplitude spectrum of the Model 2 reflectivity. The match in the 12-50 Hz bandwidth, in which we fit the AR model is good. The relative error in this band is around the -34 dB, which can be attributed to the additive noise level that is present in the input data and not in Model 2. The relative error both in the low- and in the high-frequency reconstruction is much higher, around -20 dB. Although the spectral peaks of the input and the reconstructed reflectivity appear to be correlated, the two amplitude spectra assume very different values outside the signal bandwidth.

Figure 6 about here.

Real data

We tested the AI reconstruction method on part of a line from a 2015 towed-streamer seismic survey in the Rockall Trough area across the UK Atlantic margin. The PSTM full-angle stack (6°-35°) is shown in Figure 7A together with the location of the wells and the interpreted horizons available. Ancillary data include a tomographic interval velocity field and a model-based AI inversion within the interval 1-5 s. All the data have been obtained

from the UK Oil and Gas Authority under the Open Government license v.3.0. High-amplitude events that are probably related to igneous lenses stand out in the section below the Top Paleocene horizon. As far as the authors are aware, no specific reservoir targets are present on this 2D line, as the line was selected only to demonstrate the advantages and the drawbacks of the CARV method with respect to a standard AI inversion approach in the early stages of prospect identification. Figure 7B displays, for reference, the AI field that was obtained by applying Gardner's relationship ($\alpha = 0.25$, $C = 310\ kg/m^3$) to the tomographic velocity field.

Figure 7 about here.

Different parameterizations of the CARV low-frequency reconstruction have been applied to a scaled version of the data. Calibrating seismic amplitudes to well-log amplitudes through synthetic tie analysis is the more accurate way to scale seismic data to the subsurface reflectivity (Veeken and Da Silva, 2004). However, we decided to estimate a global scalar for the whole section directly from the data to show the potential of the inversion even in absence of well-log control. We estimated that the AI is 1.5 10^6 rayl above the water-bottom and 8.5 10^6 rayl 100 ms below the Top Cretaceous event. The latter figure has been chosen in accordance to the values of Well 132/06 below the Top Cretaceous event, but a reasonable assumption is that the same degree of information may be available from background knowledge of the area of interest. We ran a first pass of the classical AR inversion algorithm directly on the seismic data with no constraints imposed at depth. After integration of the reconstructed (full-bandwidth) trace, we obtain an AI value 100

ms below the Top Cretaceous event which is, in general, different from our assumption of 8.5 10^6 rayl. The ratio between the section average of the AI values thus obtained, and the expected 8.5 10^6 rayl value, provides a mean to estimate the scalar s (see equation 3). Once the data amplitudes are calibrated to amplitudes pertaining to the reflectivity, the AR reconstruction is re-computed with impedance constraints at depth, with the AI derived from the tomographic interval velocity field, and with the lateral continuity constraint (μ). The CARV reconstructed reflectivity is then integrated into AI from a starting value of 1.5 10^6 rayl in the water layer. We obtained our preferred inversion result on the Rockall Through line when the signal bandwidth is in the range 5 to 40 Hz (see Figure 9A). The inspection of the amplitude spectrum of the input data (Figure 8) was used for defining the signal bandwidth. The high-cut choice is not obvious from Figure 8, but we decided to be conservative and to avoid the attenuation and dispersion effects that are more pronounced at higher frequencies and in the deepest part of the section. The amplitude spectrum is flat in the above mentioned frequency range, at least until 2000 ms below the water bottom.

Figure 8 about here.

Figure 9 shows a comparison between the combined AR-velocity (CARV) inversion (Figure 9A) and a model-based inversion available from the UK Oil and Gas Authority (Figure 9B). We name the latter solution "legacy inversion". Figure 9A is obtained by fixing the AR model order to 250 and by setting the parameter μ that governs the degree of spatial continuity in equation 22 to 0.2. The AI derived from the tomographic velocity field (Figure 7B) has been weighted in the inversion 9A by tuning the parameter (λ) from

equation 22 to 0.3 times the ratio of maximum eigenvalues of $\mathbf{G}$ and $\mathbf{L}^H\mathbf{L}$. The presence of two soft constraints on AI reduces the uncertainty and enhances the lateral continuity of the estimation at about the Top Paleocene (6 $10^6\pm$ 1 10^6 rayl) and the Top Cretaceous horizons (8 $10^6\pm$ 1.5 10^6 rayl). The lateral continuity is enhanced at about the timing of such horizons because, at those timings, similar values of AI are imposed to all the traces of the section. The impedance constraints are applied 100 ms after the picked horizons to avoid trace-to-trace artifacts that may arise after the CARV reconstruction sharpens the seismic events. If soft constraints were applied at the timings of the picked horizons, each constraint might be enforced right before the reconstructed reflector in one trace and right after the reconstructed reflector in the adjacent trace, thus leading to unreasonably different AI interval property between the two traces at about the timing of the constraint. The legacy inversion of Figure 9B was obtained by merging the low-frequency AI model, derived from well logs and interpolated in a stratigraphically conformable manner across the seismic line, to the relative AI recursively derived from the seismograms. The well AI logs were smoothed using the wavelet provided in the legacy inversion project and overlain to the inversion results within rectangular boxes. Figure 9C shows the difference between the inversion of Figure 9A and the inversion of Figure 9B. Within the water column and in the few hundred ms below the seabed the differences are due to the incorrect extrapolation of the well information in the shallowest portion of the legacy model-based solution. Shallow areas around trace 500 show significant anomalies in the CARV reconstruction (black arrows). A pinch-out, which is a feature of potential interest, is apparent in the difference section (Figure 9C) at about trace 700 and at about 3,500 ms TWT (black arrows). This feature is present in the CARV result, but not in the legacy AI inversion, probably because of the limits of the model-based approach when the well population and the number of horizons used

for extrapolating the log information are limited. On the contrary, the CARV inversion is not affected by these issues and it highlights an increase of AI underneath the pinch-out (Figure 9A) that is not evident in the tomographic velocity field (Figure 7B). Even though the pinch-out is also evident in the seismic data (Figure 7A), the additional piece of information contained in the CARV inversion is the estimate of the AI within the different layers. Figure 9B shows a hard layer (in yellow) at the depth corresponding to the pinch out. This layer extends across the section and we interpret it as being probably due to inaccurate extrapolation of the log information from a further well in the legacy model-based solution.

Figure 9 about here.

Figure 10 shows the effects of not accounting for the continuity term in the CARV reconstruction (Panel 10A), the effects of not incorporating the velocity-derived AI in the AR reconstruction (Panel 10B), and the effects of changing the AI derived from the velocity field in the CARV reconstruction (Panel 10C). Solving the inverse problem of equation 22, which is the case where lateral continuity is imposed, provides a more realistic estimate than solving the problem of equation 20, which is the case where lateral continuity is not imposed ($\mu = 0$). The unsmoothed solution in Figure 10A shows more high-frequency spatial noise (vertical stripes) with respect to the smoothed solution of Figure 9A. The solution that did not use the smoothing term in the cost function, shows few traces with unreliable AI, for instance those with AI larger than 2 10^6 rayl in the water column. These features are indicated by red arrows in Figure 10A. Figure 10B represents the classical AR inversion with two soft constraints at depth, and with an additional lateral continuity weight. The

weight ($\mu = 0.2$) has the same smoothing effect as the one adopted in Figure 9A. The incorporation of the interval velocity field is important to guide the solution toward accurate results: in absence of the velocity field information, as in Figure 10B, some deep parts of the section (at more than 4,000 ms for CDPs 1-1500) show lower AI values in comparison to those of Figure 9A. These lower AI values are comparable to much shallower formations and thus hard to justify on a geologic basis. To demonstrate the sensitivity of the CARV method to the variation of the interval velocity field, we show in Figure 10C the inversion result obtained if the tomographic-derived AI field is 5% higher than the AI field used for the inversion shown in Figure 9A. The color scale in Figure 10C does not directly represent the AI values, but it is normalized by the AI values of the inversion 9A. This color scale choice enhances the effects of weighting in the solution the AI derived from an overall faster velocity field. Only a subtle generalized increase of the low-frequency content of the AI is noticeable with respect to the solution of Figure 9A. The two soft constraints on impedance further attenuate the background AI variation at about the time of their respective horizons.

Figure 10 about here.

Figure 11 highlights the role played by the low-frequencies on the AI inversion. Figure 11A shows the 0-5 Hz components of the CARV inversion in Figure 9A, while Figure 11B shows the low-frequency model used as input for the model-based inversion 9B. Both the CARV reconstruction and the model-based inversion incorporate seismic data components higher than 5 Hz as recorded, to characterize the higher-frequencies of the AI. The CARV reconstruction of Figure 11A represents the AI information that we deem to be reliably

reconstructed from the seismic data and the tomographic velocity field. Figure 11A shows a relatively high AI layer (indicated by the red arrows) at about 500 ms below the water bottom, and a change in impedance in the bottom left corner of the section that is neither related to the velocity field (Figure 7B) nor to the AI constraints at the two selected horizons (black arrows). Figure 11A shows vertical stripes due to the incorporation of the information from the seismic events, particularly evident in the deepest part of the section. Those stripes are not present in Figure 11B, which is directly derived by a spatial extrapolation of well log data. The yellow region in the bottom of the low-frequency model of Figure 11B is probably due to the incorporation, in the legacy model, of a third well that lays outside of the 2D section that we discuss. The comparison between Figure 11A and 11B highlights the different low-frequency character that is responsible for the different mismatch of the two inversions at well locations.

Figure 11 about here.

Although the CARV reconstruction method appears to be a sensible solution for the low frequencies of AI at the scale of the entire section, the comparison of the results of Figure 9A and 9B at the two available wells, shows that the log matching is not as good as in the case of the legacy inversion. This result could be better appreciated in Figure 12, where the AI derived from well log measurements (red line) is compared to the model-based legacy inversion (blue line) and to the CARV inversion around the well location (gray lines). The poorer match of the CARV inversion to the log-derived AI is presumably due to the well log constraints used in the legacy AI inversion that the CARV method tries to incorporate

with ancillary indirect information and inferences. Table 3 shows the RMS error of the two types of inversion with respect to the well log data. The error for the CARV inversion is computed on the average of the 25 traces around the well location. At well 132/15 the modified AR solution is comparable with the legacy AI along much of the well, although a relatively large mismatch exists between about 3250-3400 ms. At well 132/06 a significant mismatch exists around 4100-4350 ms, with a dominant frequency between 2 and 5 Hz (see Figure 12). The mismatch in this frequency range is possibly due to an incorrect AR low-frequency extension along part of the well log. A further measure to assess the quality of the AI inversion could be the fraction of log data that is matched by the AI estimate within a given confidence level. If we set a threshold of the 15 % on the relative error of the estimation (with respect to the log-derived AI), we observe that the legacy model-based inversion exceeds this value for 6% of the length of Well 132/06 log and for 16% of the length of Well 132/15. The CARV inversion exceeds the same threshold for 28% of the length of Well 132/06 and for 22% of the length of Well 132/15. All the misfit measures we approached agree on the fact that the CARV inversion has a poorer match than the legacy model-based inversion to log data.

Table 3 about here.

Figure 12 about here.

DISCUSSION

The combined AR-velocity (CARV) algorithm reconstructs the main features of AI of the synthetic examples proposed. The introduction of an accurate interval velocity field is useful to direct the low frequencies of the inverted AI to more accurate values. For example, the CARV results (black lines of Figure 5D-5F-5H) reconstruct the AI of the most complex Model 2 (red) better than the classical AR results (gray lines). This statement is supported by the RMS errors of the reconstruction proposed in Table 2. Synthetic cases show the effects of not considering the wavelet shape in the inversion. In particular, Figures 5G and 5H show spurious peaks and incorrect values in the AI estimate that are more pronounced than in Figure 5C and 5D where the wavelet is properly removed before inversion. This behavior is also analytically discussed in the Appendix A with reference to an AR model of order 1. The presence of wavelet effects in the data may invalidate the AR reconstruction: care must be taken during pre-processing steps to minimize this issue within the signal band-width. Spectral analysis on long time windows (see Figure 8) may help to identify a frequency band were the energy of the single components is balanced. The CARV approach also results in features of interest in the inverted test field-dataset that are not observed in the legacy inversion, which incorporates log data. The comparison between Figure 11A and Figure 7B shows that the low frequency reconstruction of the CARV AI appears to contain more temporally and laterally varying character of possible geologic origin than the AI derived from the velocity field alone. The shallow areas that are characterized by a flat spectrum in the signal bandwidth show an interesting contribution of the AR reconstruction in revealing the higher impedance anomalies at about 500 ms below the water bottom, at about CDPs 500-2000 (Figure 11A). The lateral variation of the low-frequency components of the CARV inversion of Figure 11A is more realistic (despite the vertical stripes) than the

lateral variation of the low-frequency components of the legacy model-based inversion in Figure 11B, because it includes spatially-varying information in compliance with the seismic data. The very low-frequency differences between the two panels of Figure 11 are mainly due to the differences between the AI derived from the velocity field of Figure 7B and the very low frequencies of the legacy model-based inversion (Figure 11B), with a role played also by the AI constraints at about the two horizons where they are enforced. The spatially smooth very-low-frequency difference may account to a large extent for the differences that can be seen in Figure 9C. There is a tendency of the legacy model-based inversion to be more accurate at well locations because it was constructed to match the wells at low frequencies, while the CARV method does not incorporate the log data. Table 3 illustrates this bias, but the tie at much of the well depths is not dramatically different between the two inversion methods, as reported in the RESULTS section. Sources of error in the CARV inversion are also related to the uncertainty of the choice of the AI for the reference layer. This issue may not be solved once an interval velocity field is available for the poor accuracy of the velocity field in the shallow layers, and for the uncertainty on the reference density. For instance, Figure 7B shows some unrealistic velocities within the water-column. The estimation of the AI in the reference layer should be even more problematic for land data where there is no water column characterized by a very narrow range of AI. Furthermore, amplitudes of seismic data "are more reliable for marine than for land data" (Simm and Bacon, 2014). Even if we consider a lateral continuity term in the combined AR-velocity reconstruction, the inversion shows a trace-to-trace variability that is still not completely mitigated. The trace-to-trace variability does not prevent the interpretation from being made at the global scale of the inverted 2D section: the signature of the vertical stripes is different from the signature of the geologic features in the CARV reconstruction. Weighting a smooth interval

velocity field in the AR reconstruction also favors a laterally smooth solution. The interval velocity field weighting factor λ should be tuned by performing a sensitivity analysis of its effects on the result.

Figure 13 provides a measure of the sensitivity of the AI inversion depending on the CARV parametrization. Each of the four panels of Figure 13 shows the sample standard deviation among the AI models that can be obtained by sampling the most impacting parameters of the CARV reconstruction one at a time. The standard deviation, which is computed sample by sample for each trace of four Rockall Trough AI inversions. Figure 13A shows the sample standard deviation section that is obtained by varying the AR model order from 200 to 275, in increments of 25. The choice of the AR model order requires the knowledge that there are fewer reflectors in the section than the number of frequency components that can be resolved by the spectral estimation within the optimal bandwidth. In the real subsurface this condition is not always met. However, given that the AR models are less sensitive to model order than the ARMA models, and once ancillary information is available, the variability of the AI reconstruction that depends on this parameter is less than 2 10^6 rayl. Figure 13B shows that the sensitivity of the inversion to the scalar that transforms the relative amplitude of the seismogram into the reflectivity amplitude is also relatively small. In Figure 13B, we let the scalar vary from 50,000 to 65,000 in increments of 5,000. The limited impact of the scalar can be attributed to the use of ancillary information such as soft constraints at depth and the interval velocity field that make the reconstruction less sensitive to the input data amplitude variation. Figure 13C shows a measure of the variability that can be related to a change in the low frequency cut-off for fitting the AR model. The cut-off varies from 5 to 8 Hz in 1 Hz increments. The bandwidth choice appears to have a larger effect with respect to the other parameters, but a spectral analysis

of the dataset to be inverted could greatly reduce this kind of uncertainty. Figure 13D shows the sample standard deviation among four AI inversions that have been obtained by letting the trade-off parameter λ vary in the range 0.1 to 0.4 times the ratio between the maximum eigenvalues of matrix $\mathbf{G}$ and $\mathbf{L}^H\mathbf{L}$. The parameter λ weights in the CARV solution the interval velocity field, and its influence is more pronounced in the deepest part of the section where the recursion of equation 3 tends to provide less stable results if a classical AR approach is attempted. The variability in all the panels of Figure 13 is about one order of magnitude less than the estimated values of AI themselves. From a visual inspection of Figure 7A, the seismic events seem sparse enough for a correct AR modeling, but interference (see Figure 1) and attenuation (see Figure 8) tend to degrade the AR reconstruction. A comparison between our method and a similar formulation of the sparse-spike inversion that accounts for constraints at depth and velocity information might be beneficial to better understand the relevance of the AR approach with respect to the well-established sparse-spike low-frequency extension of seismic data. The comparison should consider the sensitivity of the results to the parametrization choice.

Figure 13 about here.

CONCLUSIONS

The combined AR-velocity method proposed here for the reconstruction of the full band of AI provides a more accurate solution than the classical AR algorithm on which it was based, at the expense of the larger amount of information required, some additional pre-conditioning work and parameter tuning. A reduced sensitivity to the parametrization

choice is demonstrated on synthetic examples characterized by sparsity in the time domain representation of the reflectivity and on a seismic section from the Rockall Trough area. Due to the hypothesis that the number of events is limited, that the acoustic impedance variation is only related to jumps at specific interfaces, and due to the necessity of a spectral estimation, the original AR reconstruction method is prone to inaccuracies. For this reason, our combined AR-velocity reconstruction method benefits from the introduction of the seismic-based interval velocity field combined with a targeted rock physics relationship for the density, resulting in a more accurate evaluation of the low frequency components of the AI with respect to the classical AR approach. Results appear encouraging on the test dataset and an insight on lateral variations of AI can be obtained even where no well log is available. The match between the proposed inversion results and log information is comparable to the legacy model-based inversion for one of the two wells of the Rockall Trough test line. The misfit of our inversion at the other well is significantly higher in a limited time-window. Not all the inversion results can be considered realistic representations of the subsurface impedance, especially due to proximity of the layer interfaces, interference, noise, residual wavelet effects, and sensitivity to the parametrization choice. Trace-to-trace vertical artifacts were unavoidable in the current implementation of our method, but further work on data pre-conditioning and the incorporation of a larger number of constraints when available, could reduce this issue. Regardless, the performance of the inversion procedure should be considered on the global scale of the test dataset where the signature of the geologic features of possible interest is different from the signature of the artifacts. Further research on field seismic data could be addressed to confirm the validity of the method in different geologic settings using data with different acquisition styles.

ACKNOWLEDGMENTS

The authors are thankful to the anonimous Reviewers and Associated Editor for their precious edits. The authors thank Gabriele Busanello for suggesting the test dataset and the UK Oil and Gas authority for granting access to it.

REFERENCES

Bertheussen, B., and B. Ursin, 1993, Estimation of reflection coefficients from zero offset field data: Geophysics, **58(11)**, 1634–1645.

Bleinstein, N., J. Cohen, and J. J. Stockwell, 2000, Mathematics of multidimensional seismic imaging, migration and inversion: Springer-Verlag New York, pp. 510.

Chen, K., and M. D. Sacchi, 2014, Making f-x projection filters robust to erratic noise: SEG Technical Program Expanded Abstracts 2014, 4371–4375.

Fahlman, G., and T. Ulrych, 1982, A new method for extimating the power spectrum of gapped data: Mon. Not. Royal Astronomic Society, **199**, 53–65.

Gardner, G. H. F., L. W. Gardner, and A. R. Gregory, 1974, Formation velocity and density - the diagnostic basics for stratigraphic traps: Geophysics, **39(6)**, 770–780.

Gholami, A., and M. D. Sacchi, 2013, Fast 3d blind seismic deconvolution via constrained total variation and GCV: SIAM Journal on Imaging Sciences, **6(4)**, 2350–2369.

Hargreaves, N., S. Treitel, and M. Smith, 2013, Frequency extension, resolution, and sparse inversion: SEG Technical Program Expanded Abstracts 2013, 3345–3349.

Hendrick, N., and S. Hearn, 1993, Evaluation of seismic trace inversion techniques: Exploration Geophysics, **24(3-4)**, 549–560.

Kay, S. M., and S. L. Marple, 1981, Spectrum analysis: a modern perspective: Proceedings of the IEEE, **69(11)**, 1380–1419.

Lesage, A.-C., J. Yao, F. Hussain, and D. J. Kouri, 2015, Low-frequency reflection-data augmentation by an inpainting method: 1d acoustic media: Geophysics, **80(4)**, R139–R153.

Liang, C., J. Castagna, and R. Z. Torres, 2017, Tutorial: Spectral bandwidth extension invention versus harmonic extrapolation: Geophysics, **82(4)**, W1–W16.

Löseth, H., L. Wensaas, M. Gading, K. Duffaut, and M. Springer, 2011, Can hydrocarbon source rocks be identified on seismic data?: Geology, **39(12)**, 1167.

Oldenburg, D. W., S. Levy, and K. Stinson, 1984, Root-mean-square velocities and recovery of the acoustic impedance: Geophysics, **49(10)**, 1653–1663.

Oldenburg, D. W., T. Scheuer, and S. Levy, 1983, Recovery of the acoustic impedance from reflection seismograms: Geophysics, **48(10)**, 1318–1337.

Ooe, M., and T. Ulrych, 1979, Minimum entropy deconvolution with an exponential transformation: Geophysical Prospecting, **27(2)**, 458–473.

Peterson, R. A., W. R. Fillippone, and F. B. Coker, 1955, The synthesis of seismograms from well log data: Geophysics, **20(3)**, 516–538.

Pisarenko, V., 1972, On the estimation of spectra by means of non-linear functions of the covariance matrix: Geophys. J. R. astr. Soc., **28**, 511–531.

Rao, T. S., 1970, The fitting of non-stationary time-series models with time-dependent parameters: Journal of the Royal Statistical Society. Series B (Methodological), **32(2)**, 312–322.

Robinson, A., 1954, Predictive decomposition of time series with applications to seismic exploration: PhD thesis, Massachusetts Institute of Technology.

Russell, B., 1988, Introduction to seismic inversion methods: Society of Exploration Geophysics.

Sacchi, M. D., and H. Kuehl, 2005, F-x ARMA filters: SEG Technical Program Expanded Abstracts 2000, 2092–2095.

Sacchi, M. D., and T. J. Ulrych, 2005, Recovery of near offsets using a f-x gap filling algorithm: SEG Technical Program Expanded Abstracts 1997, 1096–1099.

Sacchi, M. D., D. R. Velis, and A. H. Cominguez, 1994, Minimum entropy deconvolution

with frequency domain constraints: Geophysics, **59(6)**, 938–945.

Simm, R., and M. Bacon, 2014, Seismic amplitude: An interpreter's handbook: Cambridge University Prsss, pp. 271.

Soubaras, R., 1994, Signal preserving noise attenuation by the f-x projection filter: 64th Annual Inter. Mtg. Soc. Exploration Geophys., 1576–1579.

Soubaras, R., and Y. Lafet, 2011, Variable depth streamer acquisition: Broadband data for imaging and inversion: SEG Technical Program Expanded Abstracts 2011, 2364–2368.

Tary, J. B., R. H. Herrera, and M. van der Baan, 2014, Time-varying autoregressive model for spectral analysis of microseismic experiments and long-period volcanic events: Geophysical Journal International, **196(1)**, 600–611.

ten Kroode, F., S. Bergler, C. Corsten, J. W. de Maag, F. Strijbos, and H. Tijhof, 2013, Broadband seismic data the importance of low frequencies: Geophysics, **78(2)**, WA3–WA14.

Ulrych, T., and R. Clayton, 1976, Time series modelling and maximum entropy: Physics of the Earth and Planetary Interiors, **12(2-3)**, 188–200.

Ulrych, T. J., and C. Walker, 1984, On a modified algorithm for the autoregressive recovery of the acoustic impedance: Geophysics, **49(12)**, 2190–2192.

Veeken, P., and M. Da Silva, 2004, Seismic inversion methods and some of their constraints: First Break, **22(6)**, 47–70.

Walden, A., and J. Hosken, 1985, An investigation of the spectral properties of primary reflection coefficients: Geophysical Prospecting, **33**, 400–435.

Walker, C., and T. J. Ulrych, 1983, Autoregressive recovery of the acoustic impedance: Geophysics, **48(10)**, 1338–1350.

APPENDIX A

RESIDUAL WAVELET EFFECTS

One of the hypothesis at the basis of the AR modeling for low frequency reconstruction is that the seismic data represent a bandlimited version of reflectivity before fitting the AR model. However, on real seismic data, it is not possible to completely remove all the wavelet effects. This leads to incorrectly assume that equation 2 actually describes the recorded data. The consequences of fitting an order 1 AR model to a non-stationary complex-series is presented for the particular case where $w(t)$ is described by a Ricker wavelet with a given dominant frequency (f_d). This wavelet has the following time-domain analytic formulation:

$$w(t) = (1 - \pi {f_d}^2 t^2) e^{i2\pi^2 {f_d}^2 t^2} \tag{A-1}$$

which leads to an amplitude spectrum:

$$W(f) = \frac{2f^2}{\sqrt{\pi} {f_d}^3} e^{-\frac{f^2}{f_d^3}}. \tag{A-2}$$

In the absence of noise and for a single event r_1, equation A-1 can be rewritten as

$$d(t) = [(1 - \pi {f_d}^2 t^2) e^{i2\pi^2 {f_d}^2 t^2}] * [r_1 \delta(t - \tau_1)]. \tag{A-3}$$

Equation A-3 has the following representation in the Fourier domain

$$D(f) = \frac{2f^2}{\sqrt{\pi} {f_d}^3} e^{-\frac{f^2}{f_d^2}} r_1 e^{-i2\pi f \tau_1}. \tag{A-4}$$

In case we model equation A-4 as an AR process of order 1, the resulting AR coefficients depend on a frequency term:

$$D(f) = \frac{2(f-1)^2}{\sqrt{\pi} {f_d}^3} e^{-\frac{(f-1)^2}{f_d^2}} r_1 e^{-i2\pi(f-1)\tau_1} \frac{f^2}{(f-1)^2} e^{-\frac{f^2}{(f-1)^2}} e^{-i2\pi\tau_1}. \tag{A-5}$$

If we name $r_1 e^{-i2\pi\tau_1}$ as α_1

$$D(f) = D(f-1)\alpha_1 \frac{f^2}{(f-1)^2} e^{-\frac{f^2}{(f-1)^2}}. \tag{A-6}$$

Recursively

$$D(f) = D(f-k)\alpha_1^k \frac{f^2}{(f-k)^2} e^{-\sum_{j=1}^{k} \frac{(f-j+1)^2}{(f-j)^2}}. \tag{A-7}$$

The extension to longer AR models depends on the spectral estimator used and it is not analytically derived here. In any case, modeling the complex time-series as a stationary AR process neglects the presence of the wavelet: if the signal shows a decaying amplitude with frequency in the passband, the stationary AR model accounts for that decay and the subsequent frequency content interpolated outside the band-pass region is biased. The bias is higher when the spectral distance between the known frequencies adopted to fit the AR model to the data and the frequency to be predicted increases. For AR models of order 1, this is due to the term

$$\frac{f^2}{(f-k)^2} e^{\sum_{j=1}^{k} -\frac{(f-j+1)^2}{(f-1)^2}} \tag{A-8}$$

that increases as the distance between the frequency to be predicted (f) and the known spectral component ($f-k$) increases. The issue may find a solution by modeling the trace spectrum as a time-variant AR process (Rao, 1970), but a larger number of parameters is required.

LIST OF FIGURES

input reflectivity. Panel 5E and 5F: CARV reconstruction from input data of Panels 3A and 3B. Panel 5G and 5H: CARV reconstruction from input reflectivity convolved with a Ricker wavelet.

6 Figure 6. *Amplitude Spectra of the relative error in the reconstruction of the reflectivity of the CARV reconstruction of Figure 5F. The relative error has been obtained by dividing the reconstruction misfit by the spectrum of the input reflectivity.*

7 Figure 7. *Post-stack seismic line 78 from the Rockall Trough survey (traces 1400-6000).* *Well positions and horizons overlay the seismic section in Figure 7A. The AI [rayl] derived from tomographic velocity field and the Gardner's relationship is displayed in Figure 7B, together with AI derived from sonic and density logs.*

8 Figure 8. *Average amplitude spectrum of the Rockall Trough seismic section within three time-windows. Values are normalized to the peak amplitude.*

9 Figure 9. *Panel 9A: AI inversion [rayl] combining the AR reconstruction and the velocity field regularization term with lateral continuity. Panel 9B: model-based legacy AI estimate [rayl]. Panel 9C: difference between the CARV inversion (9A) and the model-based legacy inversion (9B) [rayl].*

10 Figure 10. *Effects of lateral continuity and ancillary information on the CARV inversion. Panel 10A [rayl] shows the result in absence of lateral smoothing, Panel 10B [rayl] shows the results of a classical AR inversion in absence of the AI derived from the velocity field. Panel 10C shows the ratio between the AI inversion when the AI derived from the tomographic velocity field is arbitrarily increased by 5%, and the AI inversion of Figure 9A.*

11 Figure 11. *Comparison between the low frequency content of AI reconstructed via the CARV method (11A) [rayl] and via the low-frequency model for the legacy inversion*

(11B) [rayl].

12 Figure 12. *AI reconstruction around the two well locations referring to the inversions presented in Figure 9A and 9B. The CARV inversion is proposed every 5 traces for 25 traces around the two well locations.*

13 Figure 13. *Sample standard deviation of the AI results among four different outputs when: the AR model order changes from 200 to 275 (13A), the scalar that maps the seismic data into reflectivity changes from 55,000 to 65,000 (13B), the low-cut frequency changes from 5 to 8 Hz (13C), the scalar that weights the velocity field changes from 0.1 to 0.4 (13D).*

LIST OF TABLES

METHOD	DESCRIPTION AND REFERENCE
Classical ARMA approach	Method adopted when the exact number of events is known a priori. Pisarenko (1972)
Unconstrained AR approach	Method described in Walker and Ulrych (1983)
Classical AR approach	Method described in Ulrych and Walker (1984)
Model-based Inversion	Method that adds the a priori low-frequencies to the bandlimited inversion. Russell (1988)
Combined AR-velocity approach (CARV)	Method described in this paper.

Table 1. Naming convention with short description of the AI inversion methods presented.

METHOD	DESCRIPTION AND REFERENCE
Classical ARMA approach	Method adopted when the exact number of events is known a priori. Pisarenko (1972)
Unconstrained AR approach	Method described in Walker and Ulrych (1983)
Classical AR approach	Method described in Ulrych and Walker (1984)
Model-based Inversion	Method that adds the a priori low-frequencies to the bandlimited inversion. Russell (1988)
Combined AR-velocity approach (CARV)	Method described in this paper

Figure	Reconstruction type	RMS error [rayl]	Figure	Reconstruction type	RMS error [rayl]
2B	ARMA order 7	47.4 10^4	2C	AR order 90	6.9 10^4
2B	ARMA order 10	4.8 10^4	2C	AR order 105	7.5 10^4
2B	ARMA order 14	18.3 10^4	2C	AR order 120	13.2 10^4
3C	Unconstrained AR	10.1 10^4	3D	Unconstrained AR	67.6 10^4
4C	Classic AR	10.1 10^4	4D	Classic AR	35.7 10^4
5C	CARV	5.3 10^4	5D	CARV	17.0 10^4
3E	Unconstrained AR	7.9 10^4	3F	Unconstrained AR	58.7 10^4
4E	Classic AR	7.9 10^4	4F	Classic AR	31.1 10^4
5E	CARV	5.0 10^4	5F	CARV	14.7 10^4
3G	Unconstrained AR	30.9 10^4	3H	Unconstrained AR	54.4 10^4
4G	Classic AR	14.3 10^4	4H	Classic AR	53.3 10^4
5G	CARV	10.3 10^4	5H	CARV	23.1 10^4

Table 2. RMS error of the synthetic reconstructions.

Figure	Reconstruction type	RMS error [rayl]	Figure	Reconstruction type	RMS error [rayl]
2B	ARMA order 7	$47.4\ 10^4$	2C	ARMA order 7	$6.9\ 10^4$
2B	ARMA order 10	$4.8\ 10^4$	2C	ARMA order 10	$7.5\ 10^4$
2B	ARMA order 14	$18.3\ 10^4$	2C	ARMA order 14	$13.2\ 10^4$
3C	Unconstrained AR	$10.1\ 10^4$	3D	Unconstrained AR	$67.6\ 10^4$
4C	Classic AR	$10.1\ 10^4$	4D	Classic AR	$35.7\ 10^4$
5C	CARV	$5.3\ 10^4$	5D	CARV	$17.0\ 10^4$
3E	Unconstrained AR	$7.9\ 10^4$	3F	Unconstrained AR	$58.7\ 10^4$
4E	Classic AR	$7.9\ 10^4$	4F	Classic AR	$31.1\ 10^4$
5E	CARV	$5.0\ 10^4$	5F	CARV	$14.7\ 10^4$
3G	Unconstrained AR	$30.9\ 10^4$	3H	Unconstrained AR	$54.4\ 10^4$
4G	Classic AR	$14.3\ 10^4$	4H	Classic AR	$53.3\ 10^4$
5G	CARV	$10.3\ 10^4$	5H	CARV	$23.1\ 10^4$

WELL	METHOD	RMS ERROR [rayl]	METHOD	RMS ERROR [rayl]
132/15	Legacy model based	57.5 10^4	Combined AR-velocity	73.4 10^4
132/06	Legacy model based	41.1 10^4	Combined AR-velocity	83.0 10^4

Table 3. RMS error of the Legacy model-based inversion and of the CARV inversion with respect to the AI measured by well logs.

WELL	METHOD	RMS ERROR [rayl]	METHOD	RMS ERROR [rayl]
132/15	Legacy model based	$57.5\ 10^4$	Combined AR-velocity	$73.4\ 10^4$
132/06	Legacy model based	$41.1\ 10^4$	Combined AR-velocity	$83.0\ 10^4$

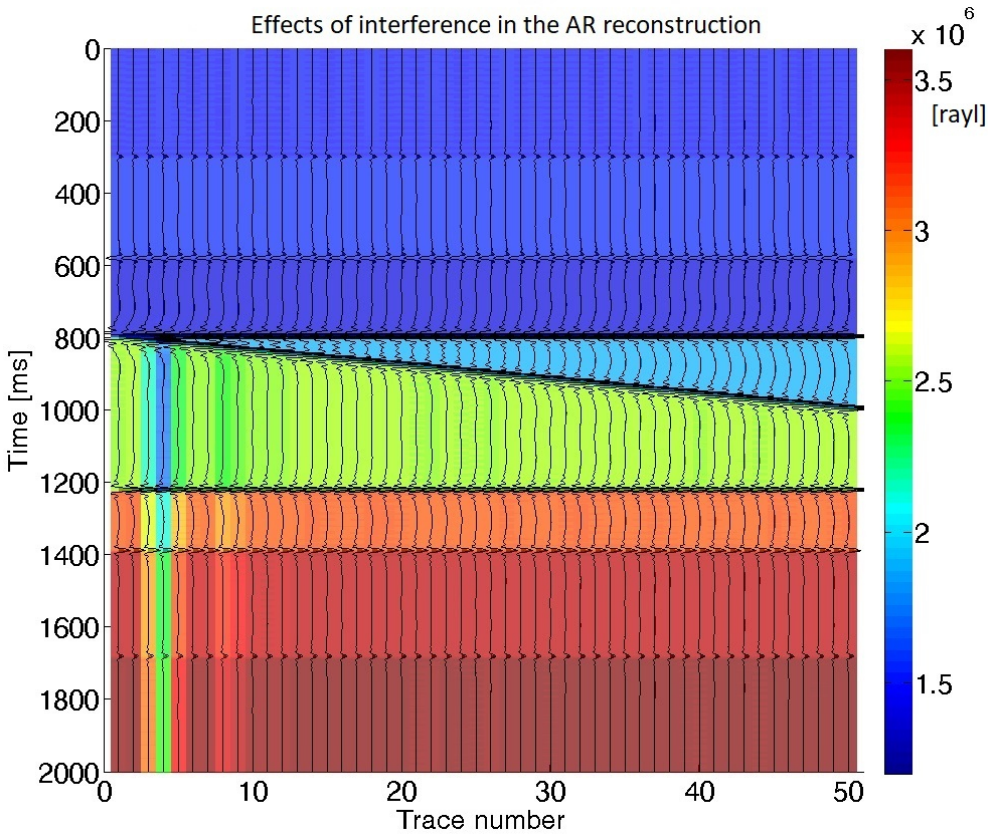

Figure 1. Synthetic wedge model that shows the effects of thin beds in the reconstruction of AI. Reconstructed AI is displayed in colors [rayl] on top of the synthetic seismic input (wiggles). Input data are bandlimited by a Butterworth zero phase filter with 7-80 Hz cut-off frequency, while the frequency band 12-50 Hz has been used for the AR modeling.

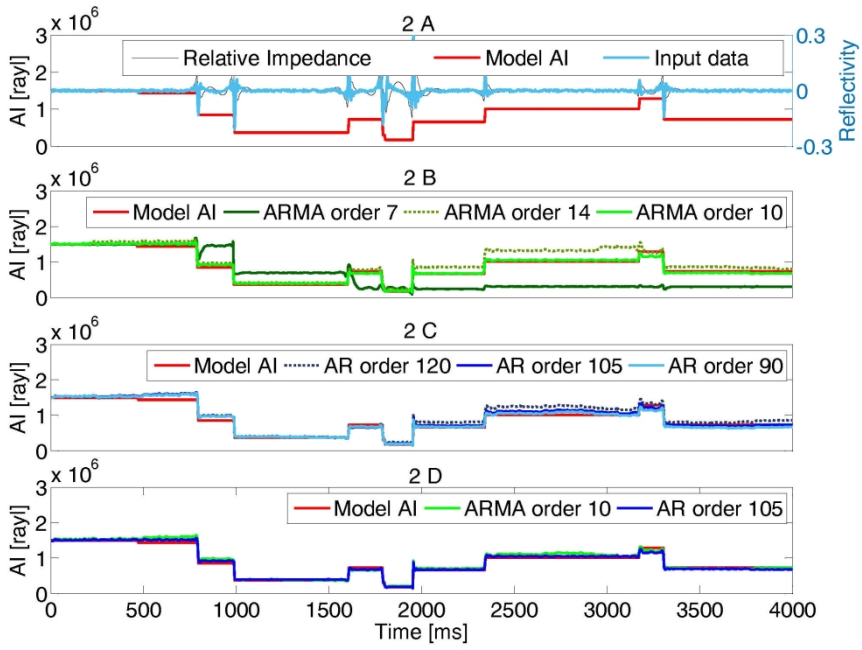

Figure 2. Results of low frequency reconstruction with AR and ARMA models. Panel 2A shows the input AI Model 1 (red) and the derived synthetic trace (cyan) (S/N = 34 dB). Panel 2B: reconstruction via unconstrained ARMA modeling. Panel 2C displays the reconstruction via the unconstrained AR modeling. Panel 2D compares the results for the two more accurate solutions of panel 2B and 2C.

297x210mm (200 x 200 DPI)

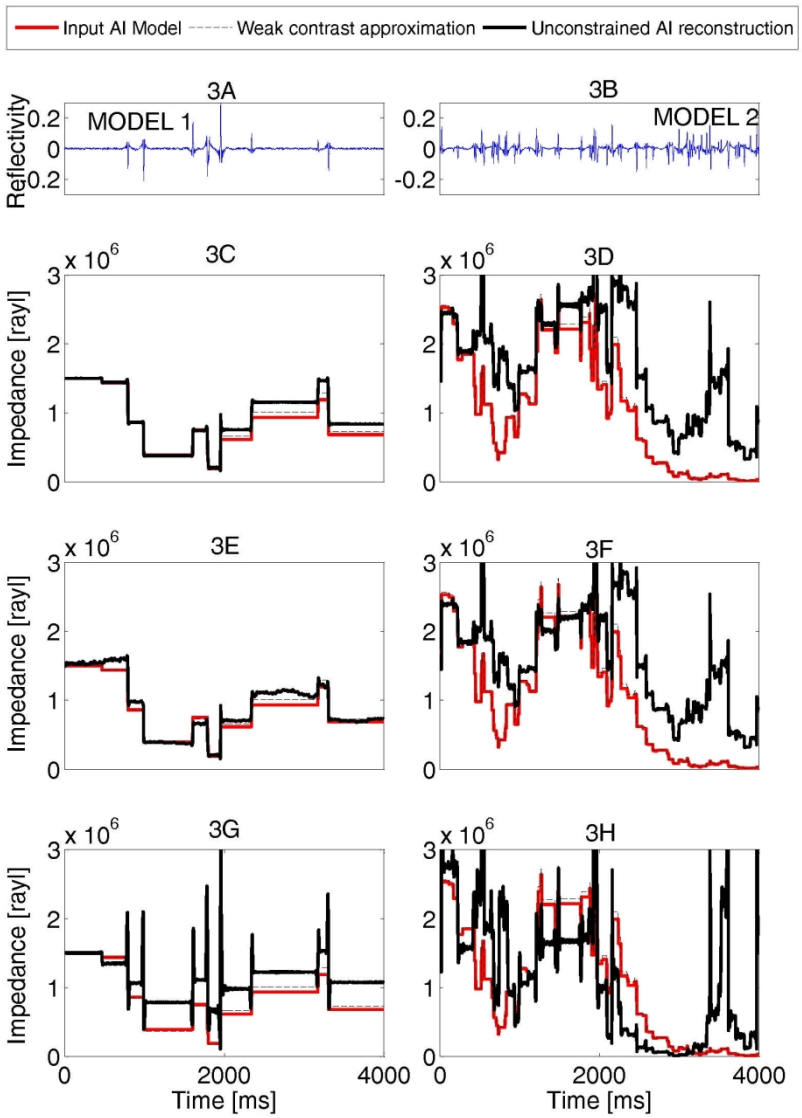

Figure 3. Effectiveness of the bandwidth extension via the AR method only. Panels 3A and 3B: input data (S/N = 34 dB). Panels 3C and 3D: reconstruction from bandlimited input reflectivity (no noise). Panels 3E and 3F: reconstruction from input data of Panels 3A and 3B. Panels 3G and 3H: reconstruction from input reflectivity convolved with a Ricker wavelet.

210x297mm (200 x 200 DPI)

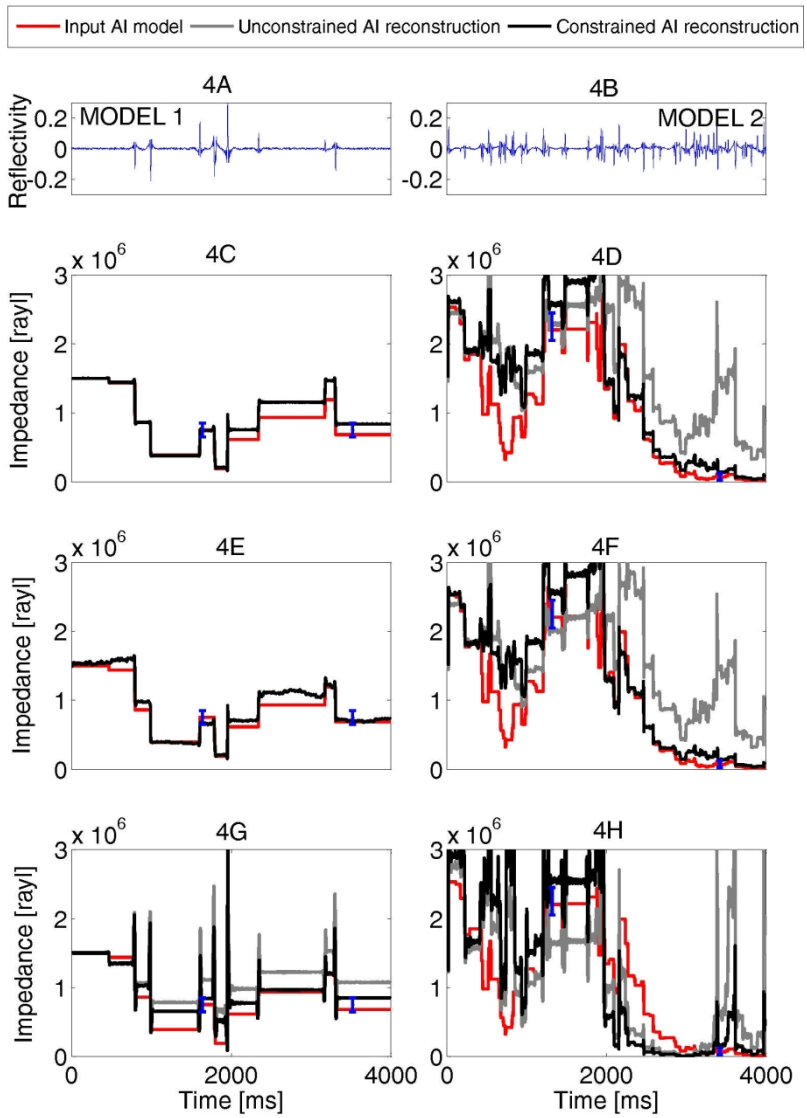

Figure 4. Effectiveness of the bandwidth extension in presence of impedance constraints at depth with a given uncertainty (in blue). Panel 4A and 4B: input data (S/N 34 dB). The unconstrained results from Figure 3 are reported in gray. Panels 4C and 4D: constrained reconstruction from bandlimited input reflectivity (no noise). Panels 4E and 4F: constrained reconstruction from input data of Panels 4A and 4B. Panels 4G and 4H: constrained reconstruction from input reflectivity convolved with a Ricker wavelet.

210x297mm (200 x 200 DPI)

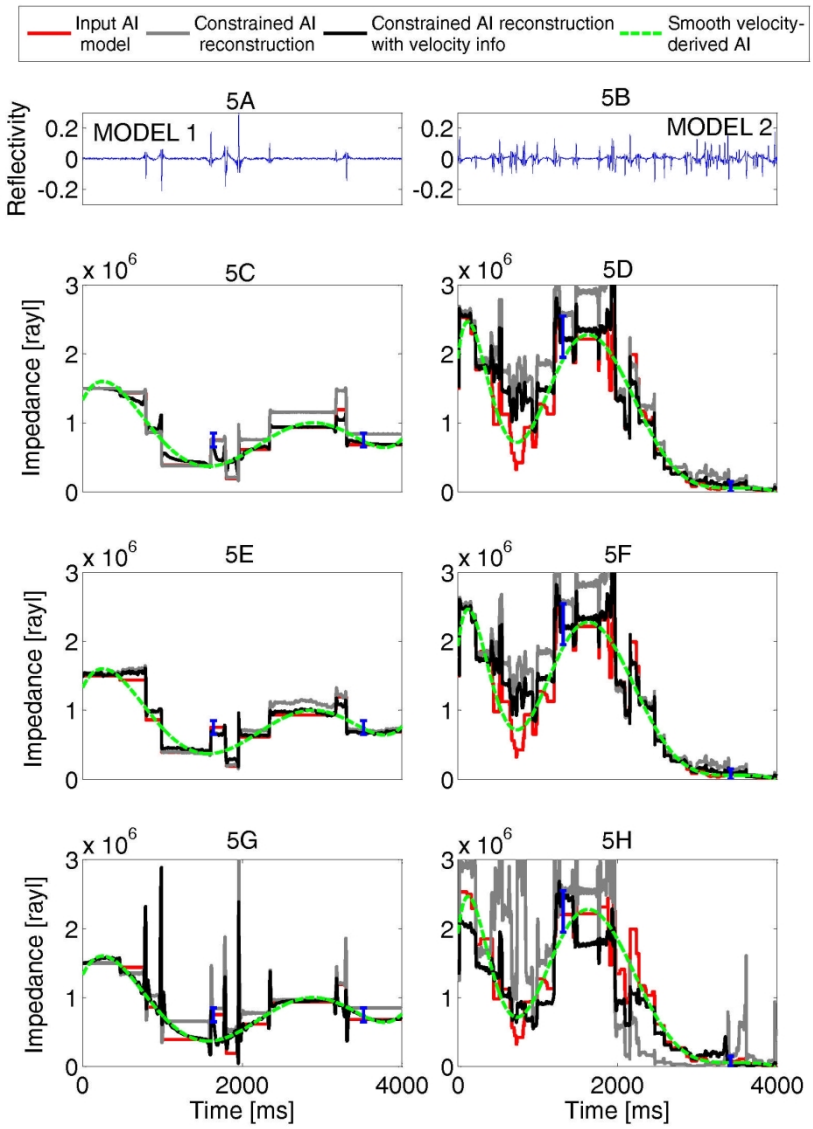

Figure 5. Results of the CARV reconstruction (black curves) and comparison with the constrained classic AR reconstruction reported in Figure 4 (gray curves). Panel 5A and 5B: input data (S/N = 34 dB). Panel 5C and 5D: CARV reconstruction from bandlimited input reflectivity. Panel 5E and 5F: CARV reconstruction from input data of Panels 3A and 3B. Panel 5G and 5H: CARV reconstruction from input reflectivity convolved with a Ricker wavelet.

210x297mm (200 x 200 DPI)

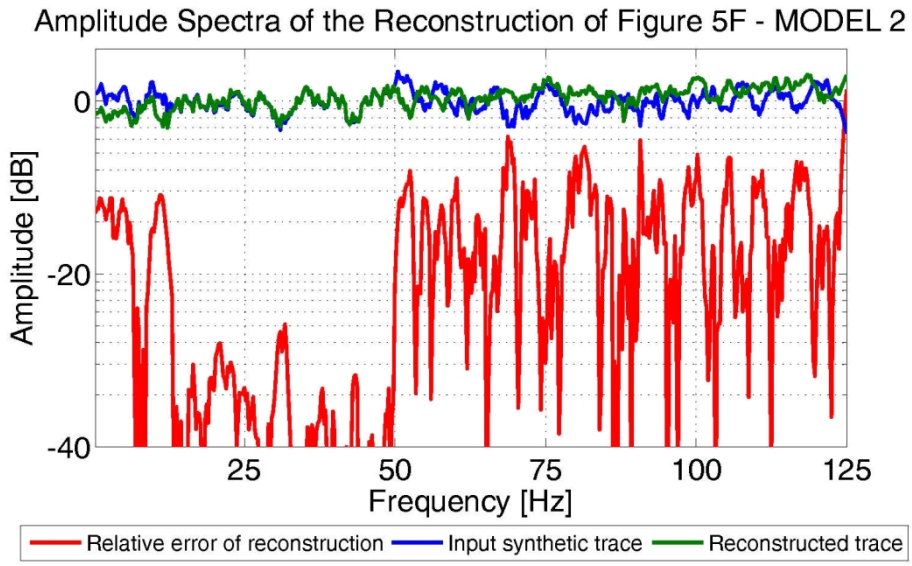

Figure 6. Amplitude Spectra of the relative error in the reconstruction of the reflectivity of the CARV reconstruction of Figure 5F. The relative error has been obtained by dividing the reconstruction misfit by the spectrum of the input reflectivity.

210x132mm (200 x 200 DPI)

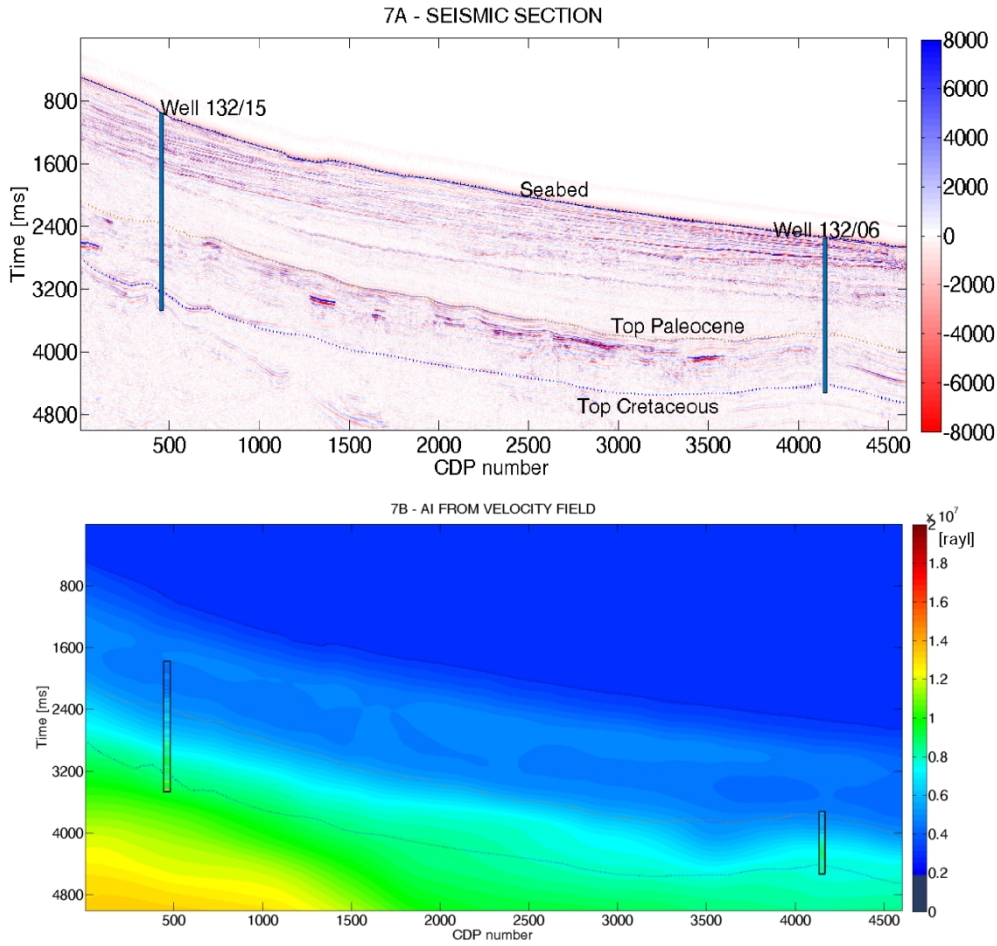

Figure 7. Post-stack seismic line 78 from the Rockall Trough survey (traces 1400-6000). © Crown Copyright. Well positions and horizons overlay the seismic section in Figure 7A. The AI [rayl] derived from tomographic velocity field and the Gardner's relationship is displayed in Figure 7B, together with AI derived from sonic and density logs.

210x202mm (300 x 300 DPI)

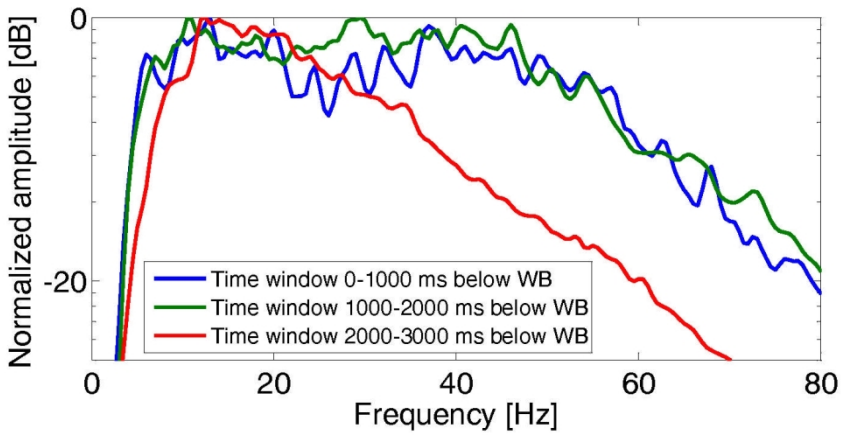

Figure 8. Average amplitude spectrum of the Rockall Trough seismic section within three time-windows. Values are normalized to the peak amplitude.

210x107mm (200 x 200 DPI)

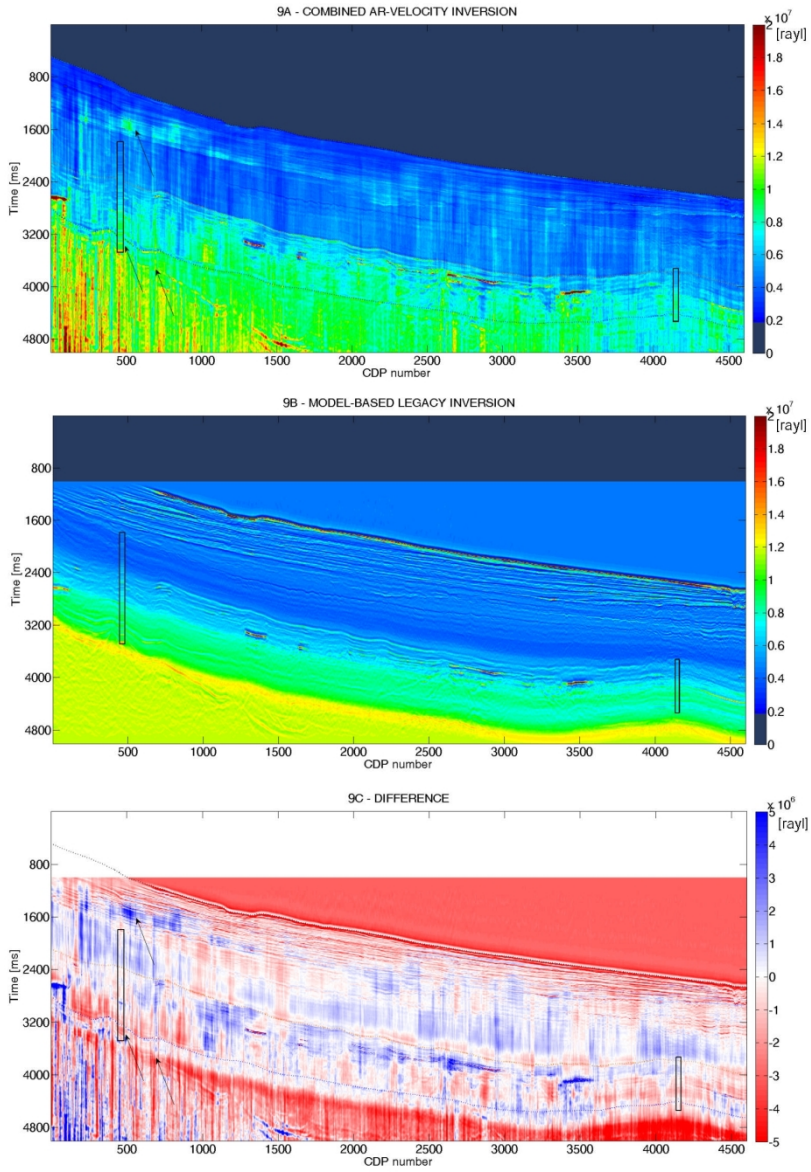

Figure 9. Panel 9A: AI inversion [rayl] combining the AR reconstruction and the velocity field regularization term with lateral continuity. Panel 9B: model-based legacy AI estimate [rayl]. Panel 9C: difference between the CARV inversion (9A) and the model-based legacy inversion (9B) [rayl].

210x297mm (200 x 200 DPI)

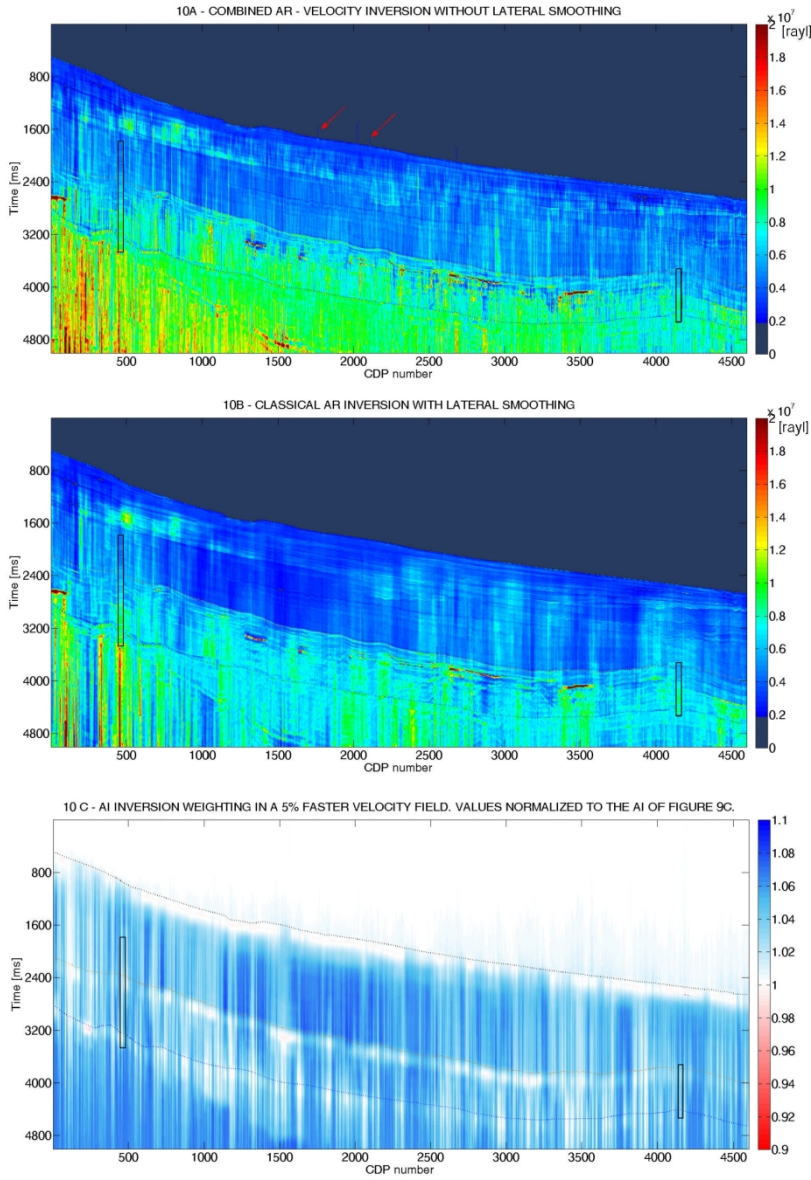

Figure 10. Effects of lateral continuity and ancillary information on the CARV inversion. Panel 10A [rayl] shows the result in absence of lateral smoothing, Panel 10B [rayl] shows the results of a classical AR inversion in absence of the AI derived from the velocity field. Panel 10C shows the ratio between the AI inversion when the AI derived from the tomographic velocity field is arbitrarily increased by 5\%, and the AI inversion of Figure 9A.

210x297mm (200 x 200 DPI)

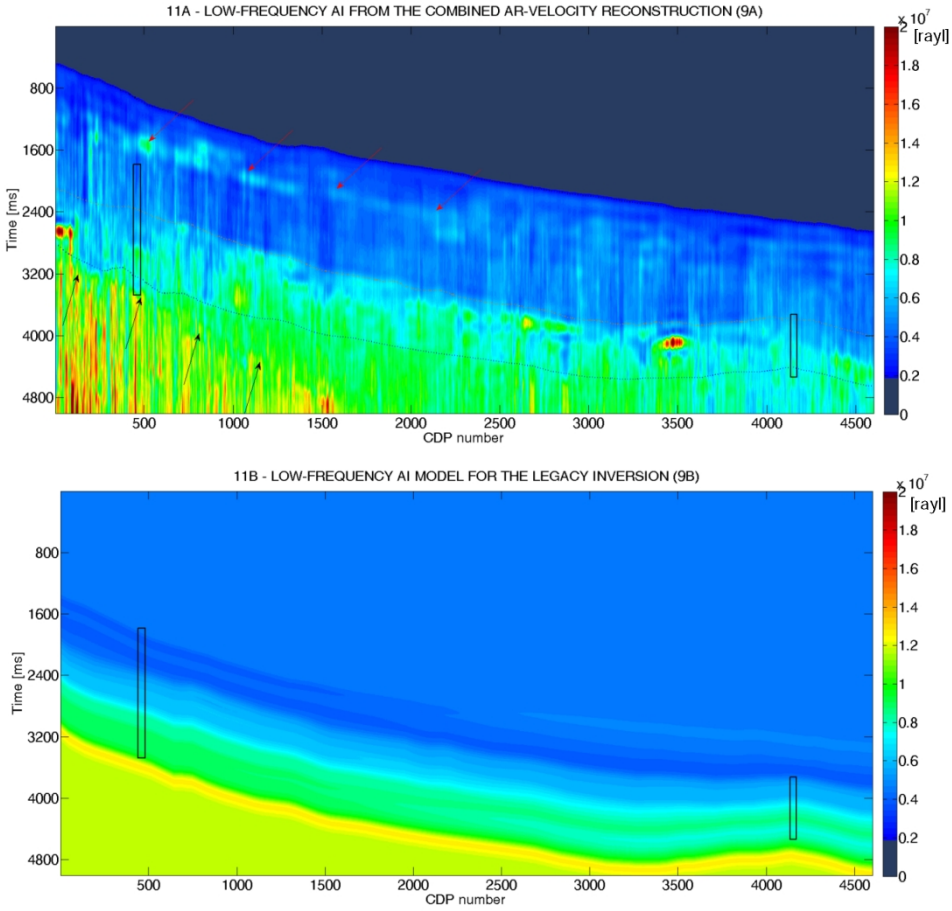

Figure 11. Comparison between the low frequency content of AI reconstructed via the CARV method (11A) [rayl] and via the low-frequency model for the legacy inversion (11B) [rayl].

210x197mm (300 x 300 DPI)

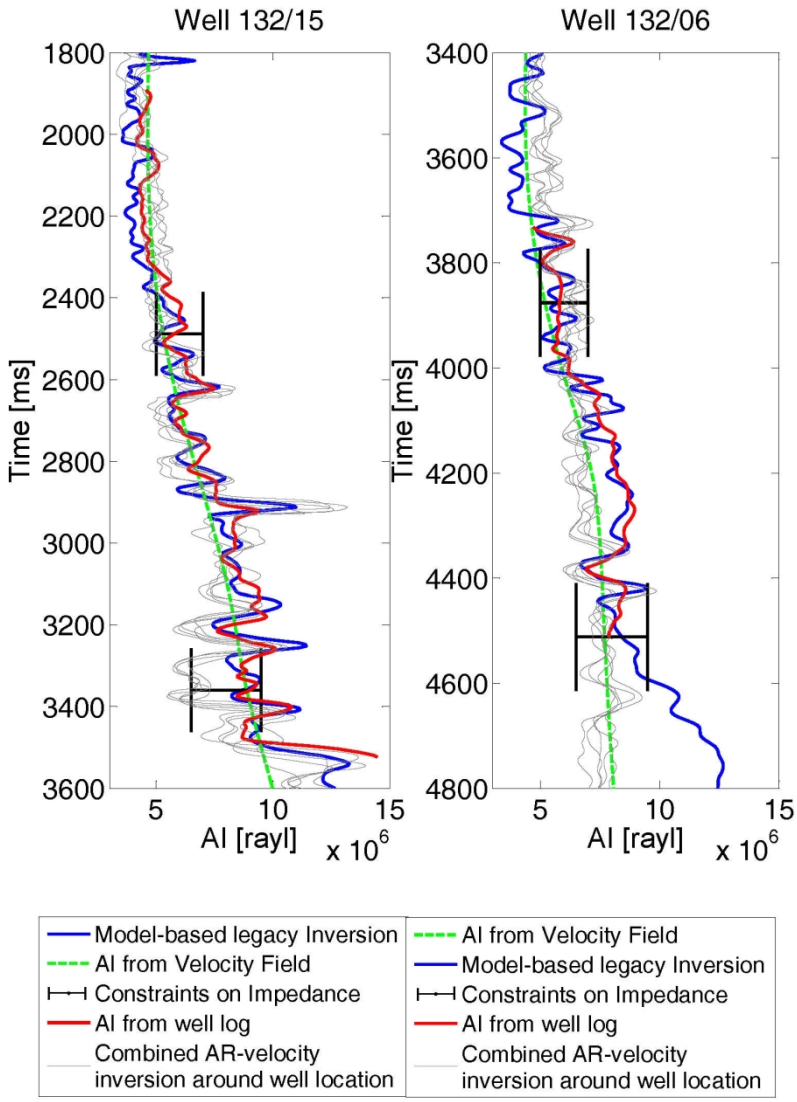

Figure 12. AI reconstruction around the two well locations referring to the inversions presented in Figure 9A and 9B. The CARV inversion is proposed every 5 traces for 25 traces around the two well locations.

210x297mm (200 x 200 DPI)

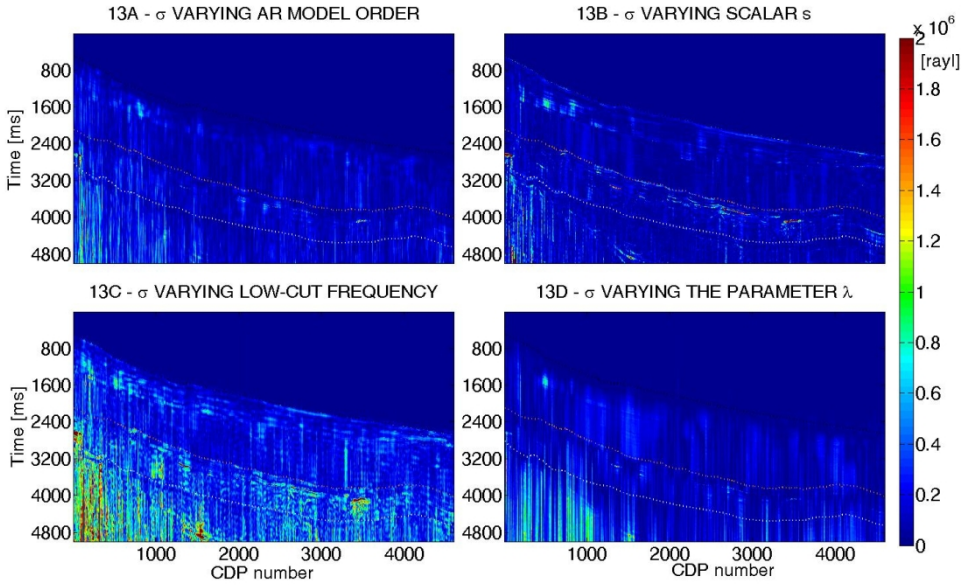

Figure 13. Sample standard deviation of the AI results among four different outputs when: the AR model order changes from 200 to 275 (13A), the scalar that maps the seismic data into reflectivity changes from 55,000 to 65,000 (13B), the low-cut frequency changes from 5 to 8 Hz (13C), the scalar that weights the velocity field changes from 0.1 to 0.4 (13D).

DATA AND MATERIALS AVAILABILITY

Data associated with this research are available and can be obtained by contacting the corresponding author.